Particuology 12 (2014) 64–79

Contents lists available at ScienceDirect

Particuology

journal homepage: www.elsevier.com/locate/partic

Effects of polydispersity on the micro–macro behavior of granular assemblies under different deformation paths

Nishant Kumar*, Olukayode I. Imole, Vanessa Magnanimo, Stefan Luding

Multi Scale Mechanics (MSM), Faculty of Engineering Technology, MESA+, University of Twente, P.O. Box 217, 7500 AE Enschede, The Netherlands

ARTICLE INFO

Article history:
Received 25 March 2013
Received in revised form 5 July 2013
Accepted 15 July 2013

Keywords:
Polydispersity
Anisotropy
Deformations
Calibration
PARDEM

ABSTRACT

The micromechanical and macromechanical behavior of idealized granular assemblies, made by linearly elastic, frictionless, polydisperse spheres, are studied in a periodic, triaxial box geometry, using the discrete element method. Emphasis is put on the effect of polydispersity under purely isotropic loading and unloading, deviatoric (volume conserving), and uniaxial compression paths.

We show that scaled pressure, coordination number and fraction of rattlers behave in a very similar fashion as functions of volume fraction, irrespective of the deformation path applied. Interestingly, they show a systematic dependence on the deformation mode and polydispersity via the respective jamming volume fraction. This confirms that the concept of a single jamming point has to be rephrased to a range of variable jamming points, dependent on microstructure and history of the sample, making the jamming volume fraction a state-variable.

This behavior is confirmed when a simplified constitutive model involving structural anisotropy is calibrated using the purely isotropic and deviatoric simulations. The basic model parameters are found to depend on the polydispersity of the sample through the different jamming volume fractions. The predictive power of the calibrated model is checked by comparison with an independent test, namely uniaxial compression. The important features of the uniaxial experiment are captured and a qualitative prediction for the evolution of stress and fabric is shown involving a "softening" regime in both stress and fabric – stronger for the latter – that was not prescribed into the model a priori.

1. Introduction and background

Granular materials are widely used as raw materials in various industrial applications, including pharmaceutical, mining, chemical, agricultural, household products, and food sectors. Processes involving milling, segregation, fragmentation, agglomeration, filtration, and sieving, among others are common and often lead to the generation of granular systems with large size ratios. The optimization of these systems is exceptionally challenging and often requires heuristic assumptions to be made. It is known, however, that polydispersity influences the micro-mechanical behavior of granular systems. For example, the shear strength and packing fraction, which are important quantities in determining the stress state and response of granular assemblies, have been shown to be influenced by the size ratio of the packing (Göncü & Luding, 2013; Shaebani, Madadi, Luding, & Wolf, 2012).

On the other hand, the bulk macroscopic behavior of granular systems originates from the contact force network between their constituent particles. The contact force networks, even for systems with uniform size distribution, are mostly inhomogeneous leading to many interesting phenomena (Shaebani et al., 2012). In recent studies involving the effects of polydispersity, emphasis has been placed on systems with narrow size distributions – ostensibly to limit the effects of long-range structural order – with the exception of a few cases where wider distributions have been reported (Dodds & Weitz, 2002; Ogarko & Luding, 2012, 2013; Voivret, Radjaï, Delenne, & El Youssoufi, 2007, 2009).

Additionally, a micromechanical description, which takes into account the discrete nature of granular systems, is necessary and must be linked to the continuum description, which involves the formulation of constitutive relations for macroscopic fields. In recent years, several constitutive relations have been proposed in literature (see Goddard, 1998, 2010; Kolymbas, Herle, & von Wolffersdorff, 1995; Mašín, 2012; Sun & Sundaresan, 2011; Thornton & Zhang, 2010 among others), but only few take into account the anisotropy that develops when granular systems are

* Corresponding author. Tel.: +31 534894212.
E-mail address: n.kumar@utwente.nl (N. Kumar).

1674-2001/$ – see front matter
http://dx.doi.org/10.1016/j.partic.2013.07.011

subjected to shear deformation (Luding & Perdahcıoğlu, 2011; Magnanimo & Luding, 2011; Peyneau & Roux, 2008; Tejchman & Wu, 2007) and no study, to our knowledge, connects anisotropy and polydispersity. When a granular assembly is subjected to shear deformation, a buildup of shear stress is observed, along with an evolution of the structural anisotropy, which describes the creation and destruction of contacts (Ai, Chen, & Ooi, 2013; Alonso-Marroquin, Luding, Herrmann, & Vardoulakis, 2005; Azéma & Radjaï, 2012; Hareb & Doanh, 2012; Kumar, Imole, Magnanimo, & Luding, 2013; Peyneau & Roux, 2008; Radjaï, Roux, & Moreau, 1999; Schröder-Turk et al., 2010; Walsh & Tordesillas, 2004). In this sense, anisotropy represents a history-parameter for the granular assembly. For anisotropic samples, scalar quantities are not sufficient to fully represent the internal direction dependent contact structure; therefore an extra tensorial quantity has to be introduced, namely the fabric tensor (Oda, 1972; Satake, 1982). To gain more insight into the microstructure of granular materials, numerical studies on various deformation experiments can be performed (see Hanley, O'Sullivan, Byrne, & Cronin, 2012; Peyneau & Roux, 2008; Thornton, 2010; Thornton & Zhang, 2006, 2010 among others).

In this study, we perform parametric studies with the goal of understanding the effects of polydispersity on both microscopic and macroscopic behavior of granular assemblies under isotropic, uniaxial and deviatoric deformation conditions. As (scalar and tensorial) microscopic quantities, we investigate the effects of polydispersity on coordination number, fraction of rattlers and fabric. The volumetric part of fabric is the measure of the strength of contact network, while the deviatoric part gives insight on the orientation of the contact network. On the macroscopic side, we consider the effects of polydispersity on the scaled pressure and the deviatoric stress. Another goal is to calibrate a constitutive model using parameters from deviatoric volume conserving simulations and test the predictive power of the calibrated model on an independent test, namely uniaxial compression test. We propose an objective definition for deviatoric stress and deviatoric fabric in a triaxial box and present findings on their behavior as a function of deviatoric strain. The parameters obtained from pure isotropic and deviatoric deformations as functions of polydispersity and volume fraction are finally inserted into the constitutive relations to predict uniaxial deformation.

This paper is organized as follows: The simulation method and parameters used and the generalized averaging definitions for scalar and tensorial quantities are given in Section 2. The preparation and test procedures are explained in Section 3. Polydispersity is introduced in Section 4.1 and its effect on the evolution of the non-scaled pressure, coordination number and fraction of rattlers for the different deformation modes is discussed in Section 4.2. In Section 4.3, the macroscopic quantities (deviatoric stress and deviatoric fabric) and their evolution are studied as functions of polydispersity, volume fraction and deviatoric (shear) strain for the different deformation modes. Finally, these results are used to obtain/calibrate the macroscopic model parameters. Section 5 is devoted to theory, where we relate the evolution of the fabric anisotropy to that of stress and strain, as proposed in Luding and Perdahcıoğlu (2011) and Magnanimo and Luding (2011), to display the predictive quality of the calibrated model.

2. Numerical simulation

The discrete element method (DEM) (Cundall & Strack, 1979) has been used extensively in performing simulations in biaxial and triaxial geometries (Durán, Kruyt, & Luding, 2010; Kruyt, Agnolin, Luding, & Rothenburg, 2010; Luding, 2005b; Sun & Sundaresan, 2011) involving advanced contact models for fine powders (Luding, 2008; Tomas, 2001), or general deformation paths (see Alonso-Marroquin et al., 2005; Thornton, 2010; Thornton & Zhang, 2010 and references therein). In this work, however, we restrict ourselves to the simplest deformation tests – namely isotropic, uniaxial and deviatoric – and to the linear contact model without friction. Since DEM is a standard method, only the contact model parameters relevant for our simulation are briefly discussed as well as the basic system parameters.

Table 1
Summary of particle parameters used in the DEM simulations.

Parameter	Symbol	Value	Value in SI units
Time unit	t_u	1	1 μs
Length unit	l_u	1	1 mm
Mass unit	m_u	1	1 μg
Number of particles	N	9261	
Average particle radius	$\langle r\rangle$	1	1 mm
Polydispersity	$w = r_{max}/r_{min}$	1–10	
Particle density	ρ	2000	2000 kg/m^3
Normal stiffness	k	10^5	10^8 kg/s^2
Normal viscosity	γ	1000	1 kg/s
Background viscosity	γ_b	100	0.1 kg/s

The simplest normal contact force model, which takes into account excluded volume and dissipation, linear repulsive and linear dissipative forces, is given as $\mathbf{f}_n = f_n\hat{\mathbf{n}} = (k\delta + \gamma\dot{\delta})\,\hat{\mathbf{n}}$, where k is the spring stiffness, γ is the contact viscosity parameter, δ is the overlap and $\dot{\delta}$ is the relative velocity in the normal direction $\hat{\mathbf{n}}$. An artificial background dissipation force, $\mathbf{f}_b = -\gamma_b\mathbf{v}_i$, proportional to the velocity $\mathbf{v}_i$ of particle i is added, resembling the damping due to a background medium, as e.g. a fluid. A short summary of the values of the parameters used in DEM simulations is shown in Table 1. Note that the units are artificial and can be consistently rescaled to quantitatively match the values obtained from experiments (due to the simplicity of the contact model used), as shown in (Luding, 2008). We want to point out here that the choice of contact model (linear or non-linear) affects the collisional behavior between two particles as well as the bulk behavior (Ji & Shen, 2006; Shäfer, Dippel, & Wolf, 1996). When linear and hertzian contact models are compared, a major difference is related to the initial contact stiffness, where the former presents a finite constant value, while for the later, the stiffness is a function of the deformation, namely it is zero at the beginning. However, the difference between the two models become smaller when the consolidation pressure becomes higher, as is the case in this study.

2.1. Microscopic variables

In order to link the macroscopic load carried by the sample with the active microscopic contact network, all particles that do not contribute to the force network are excluded from the computation. Frictionless particles with less than 4 contacts are thus "rattlers", since they cannot be mechanically stable and hence do not contribute to the contact network (Göncü, Duran, & Luding, 2010; Imole, Kumar, Magnanimo, & Luding, 2013a; Madadi, Tsoungui, Latzel, & Luding, 2004). The simple definition of coordination number is $C = M/N$, where M is the total number of contacts and $N = 9261$ is the total number of particles. If the overlap at a contact between two particles is greater than or equal to zero, i.e., $\delta \geq 0$, the contact contributes to the force network. The corrected coordination number is $C^* = M_4/N_4$, where M_4 is the total number of contacts of the N_4 particles with at least 4 contacts, and the rattler fraction is $\phi_r = (N - N_4)/N$.

The total volume of particles is $\sum_{p=1}^{N} V_p = 4\pi N\langle r^3\rangle/3$, where $\langle r^3\rangle/3$ is the third moment of the size distribution discussed in detail in Section 4.1 and the volume fraction is defined as $\nu = (1/V)\sum_{p=1}^{N} V_p$, where V is the volume of the box. Note that for

the calculation of the total volume of particles, the volume which should be subtracted due to particle overlaps is neglected.

2.2. Macroscopic variables

Here, we focus on defining averaged macroscopic tensorial quantities, including strain, stress and fabric (structure) tensors, that reveal interesting bulk features and provide information about the state of the packing due to its deformation.

For any deformation, we can describe the externally applied strain through the infinitesimal strain tensor **E**. Its isotropic part ε_v (Göncü et al., 2010; Imole et al., 2013a) is defined as:

$$\varepsilon_v = \dot{\varepsilon}_v\, dt = \frac{\varepsilon_{xx}+\varepsilon_{yy}+\varepsilon_{zz}}{3} = \frac{1}{3}\mathrm{tr}(\mathbf{E}) = \frac{1}{3}\mathrm{tr}(\dot{\mathbf{E}})\, dt, \tag{1}$$

where $\varepsilon_{\alpha\alpha} = \dot{\varepsilon}_{\alpha\alpha}\, dt$ with $\alpha\alpha = xx, yy$ and zz as the diagonal elements of **E** in the Cartesian x, y, z reference system. The trace integral of $3\varepsilon_v$, denoted as the volumetric strain ε_v is the true or logarithmic strain, i.e., the volume change of the system relative to the initial reference volume, V_0.

From the DEM simulations, one can determine the stress tensor as

$$\boldsymbol{\sigma} = \frac{1}{V}\sum_{c\in V} \mathbf{l}^c \otimes \mathbf{f}^c, \tag{2}$$

which is an average over the contacts in the volume V of the dyadic products between the branch vector $\mathbf{l}^c$ and the contact force $\mathbf{f}^c$, where the contribution of the kinetic energy has been neglected (Luding, 2005a). The isotropic component of the stress is the pressure $P = \mathrm{tr}(\boldsymbol{\sigma})/3$.

Besides the stress, we will focus on the fabric tensor in order to characterize the geometry/structure of the static aggregate, defined as

$$\mathbf{F} = \frac{1}{V}\sum_{P\in V} V^P \sum_{c\in P} \mathbf{n}^c \otimes \mathbf{n}^c, \tag{3}$$

where V^P is the volume of particle P, which lies inside the averaging volume V, and $\mathbf{n}^c$ is the normal unit branch-vector pointing from center of particle P to contact c (Kumar et al., 2013; Luding, 2005a). The average isotropic fabric is $F_v = \mathrm{tr}(\mathbf{F}) = g_3 \nu C$, where ν and C are, respectively, the volume fraction and the coordination number, and g_3 is a function of moments of the size distribution (Göncü et al., 2010; Shaebani et al., 2012), as explained in detail in Section 4.1. We want to highlight here that a different formulation for the fabric tensor considers simply the average orientation of contacts as follows (Oda, 1972; Satake, 1982):

$$\mathbf{F}^s = \frac{1}{N_c}\sum_{c\in N_c} \mathbf{n}^c \otimes \mathbf{n}^c, \tag{4}$$

where N_c is the total number of contacts. The relationship between Eqs. (3) and (4) is:

$$\mathbf{F}^s \approx \frac{\mathbf{F}}{g_3 \nu C} = \frac{3\mathbf{F}}{F_v}, \tag{5}$$

where the equality holds for the monodisperse case.

In addition to the isotropic components, we use the following definition to quantify the magnitude of the deviatoric parts (Kumar et al., 2013) of tensors **Q** (stress $\boldsymbol{\sigma}$, strain **E** or fabric **F**):

$$Q_{dev} = \mathrm{Fsgn}(\mathbf{Q})\sqrt{\frac{(Q_{xx}-Q_{yy})^2+(Q_{yy}-Q_{zz})^2+(Q_{zz}-Q_{xx})^2+6(Q_{xy}^2+Q_{yz}^2+Q_{zx}^2)}{2}}, \tag{6}$$

where Q_{xx}, Q_{yy}, and Q_{zz} are the diagonal components, and Q_{xy}, Q_{yz}, and Q_{zx} are the off-diagonal components of the symmetric tensor **Q**. Fsgn(**Q**) is the sign function with possible values +1, 0, and −1, whose definition depends on the deformation path (see Section 4.3). In the case of stress, Eq. (6) equals the von Mises stress, $\sigma_{dev} = \sqrt{3J_2}$, with J_2 as the second deviatoric stress invariant.

When a biaxial or triaxial compression is performed, such that the strain, stress and fabric stay almost coaxial with principal axes parallel to the initial reference system, the off-diagonal terms become negligible and the diagonal terms coincide with the eigenvalues.

3. Preparation and test procedure

After the (common) initial isotropic preparation, the packing is deformed following three different procedures, namely isotropic, uniaxial, and deviatoric paths (a detailed procedure can be found in Imole et al., 2013a). For convenience, the definitions of the different modes will be based on their respective strain-rate tensors. Also note that the deformations applied to systems are always "slow" enough to maintain the quasi-static regime and hence minimize the dynamical effects (Hanley et al., 2012; Imole et al., 2013a).

3.1. Initial isotropic preparation

Since careful, well-defined sample preparation is essential in any physical experiment to obtain reproducible results, the preparation consists of three parts: (i) randomization, (ii) isotropic compression, and (iii) relaxation, all equally important to achieve the initial configurations for the subsequent analysis. (i) The initial configuration is such that spherical particles are randomly generated in a 3D box without gravity, with low volume fraction and rather large random velocities, such that they have sufficient space and time to exchange places and to randomize themselves. (ii) This granular assembly is then isotropically compressed, in order to approach a direction independent initial configuration with target volume fraction $\nu_0 = 0.64$, slightly below the jamming volume fraction, i.e. the transition point from fluid-like behavior to solid-like behavior (Majmudar, Sperl, Luding, & Behringer, 2007; Makse, Johnson, & Schwartz, 2000; O'Hern, Langer, Liu, & Nagel, 2002; van Hecke, 2010). (iii) This is followed by a relaxation period at constant volume fraction to allow the particles to fully dissipate their energy and to achieve a static configuration in mechanical equilibrium, after sufficient relaxation indicated by the drop in kinetic to potential energy ratio to almost zero.

3.2. Isotropic compression mode

Further isotropic compression (negative strain-rate in our convention) can now be used to prepare initial configurations at different volume fractions, each one with subsequent relaxation, achieved at different steps during loading and unloading, as displayed in Fig. 1. Furthermore, this path can be considered as the isotropic element test by itself (Göncü et al., 2010). It is realized by a simultaneous inward movement of all the periodic boundaries of the system, with diagonal strain rate tensor

$$\dot{\mathbf{E}} = \dot{\varepsilon}_v \begin{pmatrix} -1 & 0 & 0 \\ 0 & -1 & 0 \\ 0 & 0 & -1 \end{pmatrix},$$

where $\dot{\varepsilon}_v (> 0)$ is the rate amplitude applied to the walls until the target maximum volume fraction $\nu_{max} = 0.82$ is achieved. The simulations are continued with negative $\dot{\varepsilon}_v$ in the unloading mode, until the initial ν_0 is reached. The unloading branch configurations are

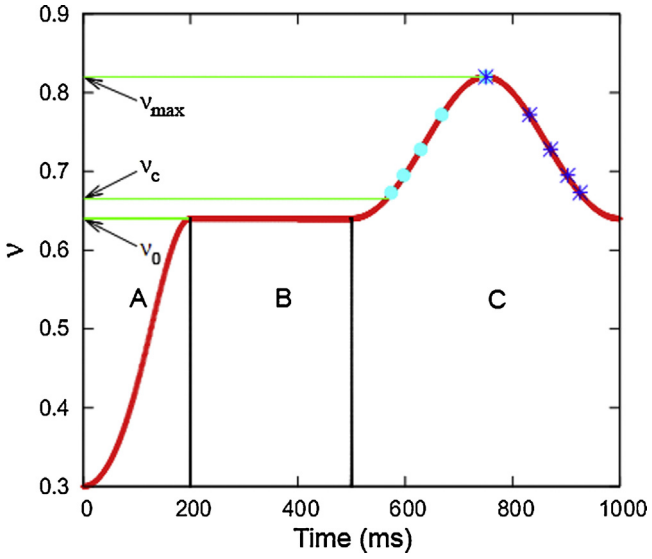

Fig. 1. Evolution of volume fraction as a function of time. Region A represents the initial isotropic compression below the jamming volume fraction ν_c. B represents relaxation of the system to fully dissipate the systems energy and C represents the subsequent isotropic compression up to $\nu_{max} = 0.820$ and then decompression. Cyan dots represent some of the initial configurations, at different ν_i, during the loading cycle and blue stars during the unloading cycle, at the same ν_i, which can be chosen for further study (see Imole et al. (2013a) for more details).

more reliable since this part of the deformation is much less sensitive to the protocol and rate of deformation during preparation (Göncü et al., 2010; Imole et al., 2013a). Consequently, we will use those initial states for our analysis.

3.3. Uniaxial compression mode

Uniaxial compression is one of the element tests that is initiated at the end of the "preparation". The uniaxial compression mode in the triaxial box is achieved by a prescribed strain path in the z-direction, while the other boundaries x and y are non-mobile. During loading (compression) the volume fraction increases, like for isotropic compression, from $\nu_0 = 0.64$ to a maximum volume fraction of $\nu_{max} = 0.820$ (as shown in region C of Fig. 1), and reverses back to the original volume fraction ν_0 during unloading. Uniaxial compression is defined by the strain-rate tensor

$$\dot{\mathbf{E}} = \dot{\varepsilon}_u \begin{pmatrix} 0 & 0 & 0 \\ 0 & 0 & 0 \\ 0 & 0 & -1 \end{pmatrix},$$

where $\dot{\varepsilon}_u$ is the strain-rate (compression > 0 and decompression/tension < 0) amplitude applied. The negative sign (convention) of $\dot{E}_{zz}$ corresponds to a reduction of length, so that tensile deformation is positive. Even though the strain is imposed only on the mobile "wall" in the z-direction, which leads to an increase of compressive stress on this wall during compression, also the non-mobile walls experience some stress increase due to the "push-back" stress transfer and rearrangement of the particles during loading, as discussed in more detail in the following sections. This is in agreement with theoretical expectations for solid materials with non-zero Poisson's ratio. However, the stress on the passive walls is typically smaller than that of the mobile, active wall, as consistent with findings from laboratory element tests using the biaxial tester (Morgeneyer & Schwedes, 2003; Zetzener & Schwedes, 1998) or the so-called λ-meter (Kwade, Schulze, & Schwedes, 1994a,b).

3.4. Deviatoric deformation mode

The preparation procedure, as described in Section 3.1, provides different configurations with volume fractions ν_i. Starting from the values ν_i in the unloading branch of the isotropic path as shown in Fig. 1, we perform volume conserving deviatoric deformations with strain-rate tensor

$$\dot{\mathbf{E}} = \dot{\varepsilon}_{D2} \begin{pmatrix} 1 & 0 & 0 \\ 0 & 0 & 0 \\ 0 & 0 & -1 \end{pmatrix},$$

where $\dot{\varepsilon}_{D2}$ is the strain-rate (compression > 0) amplitude applied to the wall with normal in z-direction. The chosen deviatoric path is on the one hand similar to the pure-shear situation, and on the other hand allows for simulation of the biaxial experiment (with two walls static, while four walls are moving (Morgeneyer & Schwedes, 2003; Zetzener & Schwedes, 1998)), in contrast to the more difficult isotropic compression, where all the six walls are moving. (Pure shear is here used to identify constant volume deviatoric loading with principal strain axis keeping the same orientation as the geometry (cubical) of the system for the whole experiment. In this case, there is no rotation (vorticity) of the strain principal axis and no distortion/rotation of the sample due to deformation.) Different types of volume conserving deviatoric deformations can be applied to shear the system, but very similar behavior has been observed (Imole et al., 2013a).

4. Polydispersity

Most granular materials are highly polydisperse in nature. It is known that size polydispersity affects the mechanical behavior of granular systems (e.g., shear strength) as well as their space-filling properties (e.g., packing fraction) (Göncü & Luding, 2013; Ogarko & Luding, 2012, 2013), which are crucial in many engineering applications like road construction or soils liquefaction problems (see (Anderson, 1996; Belkhatir, Arab, Della, & Schanz, 2012; Belkhatir, Arab, Schanz, Missoum, & Della, 2011) and references therein). Nevertheless the attention has been restricted so far to monodisperse or binary mixtures or narrow size distribution. Here we use samples with different degrees of polydispersity to study the effect of increasing polydispersity on the evolution of microscopic and macroscopic parameters during various deformation modes.

4.1. Polydispersity of the granular assemblies studied

We define polydispersity in terms of the width $w = r_{max}/r_{min}$, where r_{max} and r_{min} represent the radii of the largest and smallest particles in the overall ensemble of a distribution uniform in size (Göncü et al., 2010; Göncü & Luding, 2013):

$$f(r) = \frac{w+1}{2(w-1)\langle r\rangle} \Theta\left(\frac{2w\langle r\rangle}{w+1} - r\right) \Theta\left(r - \frac{2\langle r\rangle}{w+1}\right), \quad (7)$$

with step function $\Theta(x \geq 0) = 1$ and $\Theta(x < 0) = 0$. From the distribution of radii, one can calculate the parameter g_3 that describes the polydispersity of a 3D spherical system (Göncü et al., 2010) as:

$$g_3 \approx \frac{1 - B_2 + C_2 + (B_2 - 2C_2)(\langle r^4\rangle/\langle r\rangle\langle r^3\rangle) + C_2(\langle r^5\rangle/\langle r\rangle^2\langle r^3\rangle)}{1 + C_2[\langle r^2\rangle/\langle r\rangle^2 - 1]}, \quad (8)$$

where the constants $B_2 = 1.077$ and $C_2 = 0.2629$ are described in Göncü et al. (2010) and $\langle r^n\rangle$ is the nth moment of r up to the 5th degree. Only for the monodisperse case, the simplification $g_3 = 1$ holds. Otherwise, g_3 increases with polydispersity w and saturates at high values about 1.627.

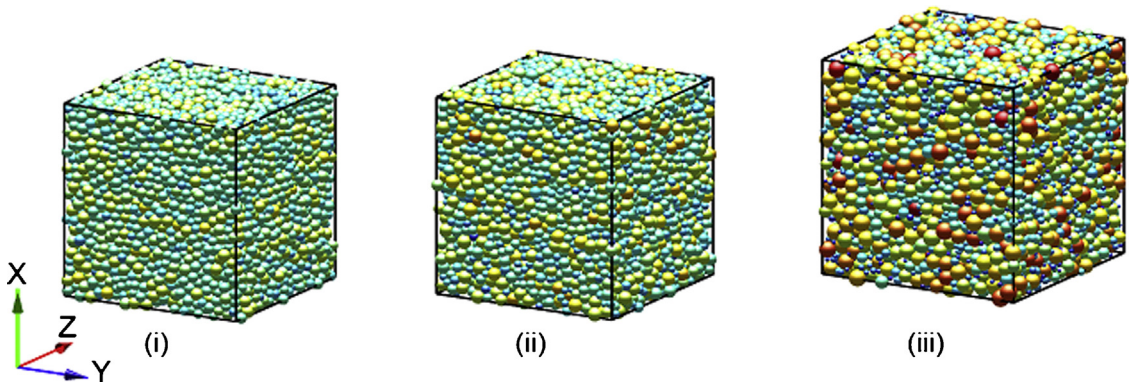

Fig. 2. Snapshots of three systems with polydispersity w equal to (i) 1.5, (ii) 2, and (iii) 5, respectively, with the same volume fraction $\nu = 0.82$. The color code indicates the contacts of the particles, with red representing big contacts, blue representing no contacts. (For interpretation of the references to color in this figure legend, the reader is referred to the web version of the article.)

In order to study the effects of polydispersity on micro–macro behavior of a granular assembly, we prepare different packings with polydispersity ranging from $w = 1$ to 10. These packings are deformed following the paths described in Section 3. As an example, we show in Fig. 2 isotropic samples with $w = 1.5$, 2, and 5 for constant volume fraction $\nu = 0.82$. Note that for the same volume fraction ν, the volume of the box is higher for higher polydispersity, since $\langle r^3 \rangle$ increases with w for fixed $\langle r \rangle = 1$. For higher polydispersity, particles of smaller size fill more efficiently the pore space between larger particles. However, lower polydispersity in packings of granular materials is associated with alterations in the structural order (Ogarko & Luding, 2012; Voivret et al., 2007). (Note that here results for a uniform radius distribution are presented. The trend will be different if the type of distribution is different e.g., uniform surface or uniform volume distribution.)

4.2. Effect of polydispersity on isotropic quantities

In the following, we will study the influence of polydispersity on scaled pressure, coordination number and fraction of rattlers, during the three deformation paths described in Section 3.

4.2.1. Confining pressure

Starting from Eq. (2), we define the non-dimensional pressure (Göncü et al., 2010; Imole et al., 2013a) as

$$p = \frac{2\langle r \rangle}{3k} \mathrm{tr}(\boldsymbol{\sigma}), \tag{9}$$

with $\langle r \rangle$ the first radius moment (average radius) and k the spring stiffness defined in Section 2, while the scaled pressure is:

$$p^* = \frac{p\nu_c}{\nu C} = p_0(-\varepsilon_v)[1 - \gamma_p(-\varepsilon_v)], \tag{10}$$

where p_0, γ_p, and the critical volume fraction ν_c are fit parameters, $-\varepsilon_v$ is the volumetric strain. When comparing the two expressions of non-dimensional and scaled pressure, we notice that in Eq. (10), the pressure is normalized by "νC", that is, the contribution of the density of contacts is canceled. Hence, p^* is only proportional to the average deformation (overlap) of the particles at a given volume fraction and to the distance from jamming point through $-\varepsilon_v$.

In Fig. 3, we plot the variation of the non-dimensional pressure p with volume fraction ν during isotropic, uniaxial, and deviatoric deformation for polydispersities $w = 1.5$ and 5. Note that p increases with ν, starting from ν_c, with slight differences related to different modes, as discussed in Imole et al. (2013a). For a given volume fraction, we observe a decrease in the pressure with increasing polydispersity w. Better insights into this feature are gained by

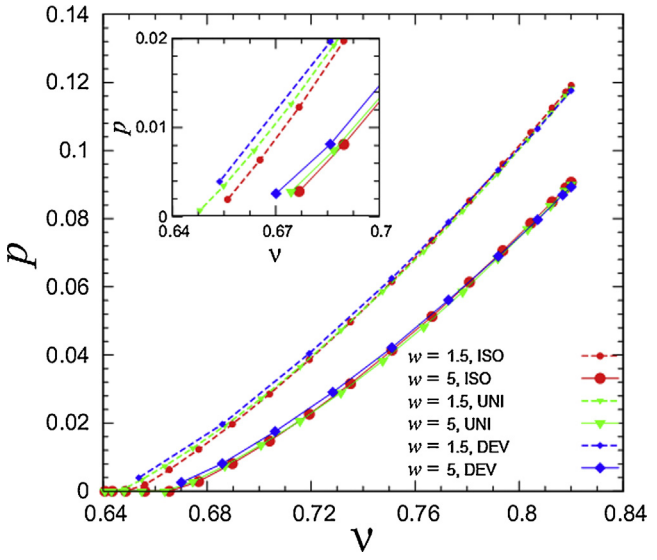

Fig. 3. Variations of non-dimensional pressure p with volume fraction ν for the isotropic (●, red), uniaxial (▼, green), and deviatoric (♦, blue) deformation modes, as shown in the legend. Small symbols represent $w = 1.5$ and big symbols represent $w = 5$. Inset is the zoomed-in area near the jamming volume fraction ν_c. (For interpretation of the references to color in this figure legend, the reader is referred to the web version of the article.)

looking at the distribution of overlaps $\delta(r)/\langle r \rangle$ as a function of the scaled particle radius $r_{sc} = (r - r_{min})/(r_{max} - r_{min})$, as shown in Fig. 4(a) and (b) for two volume fractions, $\nu = 0.686$ and $\nu = 0.82$. The particle radii are scaled such that $r_{sc} = 0$ and $r_{sc} = 1$ represent the smallest and largest particle in the configuration, respectively. A first observation is the unsurprising increase in the average overlap for all modes and polydispersities with increasing compression from $\nu = 0.686$ in Fig. 4(a) to $\nu = 0.82$ in Fig. 4(b), in agreement with Fig. 3. Based on this, we can claim that $2\langle r \rangle P/k \propto \delta(r)/\langle r \rangle$, at least for small deformations and for the linear contact model. In addition, for both volume fractions shown, the overlap increases with increasing particle radii.

Focusing on the deformation mode trend, for both polydispersities, the deviatoric deformation leads to the highest pressure, followed by the uniaxial and isotropic modes, respectively. This trend is clearly visible at lower volume fractions, as shown in the inset of Fig. 3, while for increasing volume fraction, the effect of the deformation mode reduces, as evidently shown by the collapse of data in Fig. 4(b). The agreement is confirmed by observing the average overlap $\langle \delta \rangle$ in Fig. 4(a) and (b), with the data from uniaxial

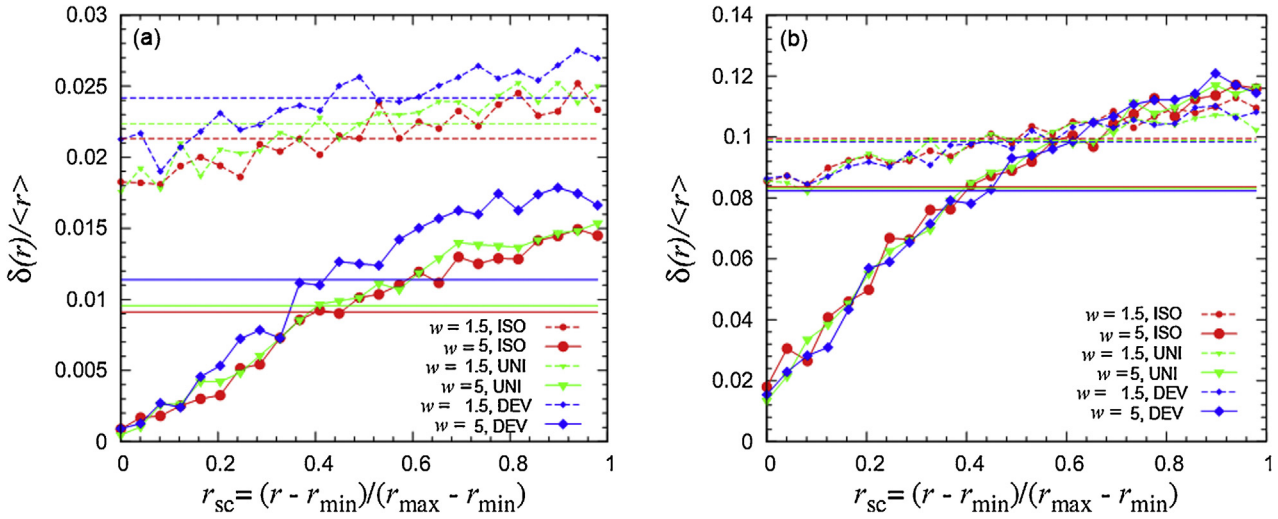

Fig. 4. Average overlap δ per particle for a radius range scaled by average radius $\langle r \rangle$, plotted against a scaled radius axis $r_{sc} = (r - r_{min})/(r_{max} - r_{min})$ for the isotropic (●, red), uniaxial (▼, green), and deviatoric (♦, blue) deformation modes. Small symbols represent $w = 1.5$ and big symbols represent $w = 5$. Volume fractions are (a) $\nu = 0.686$ and (b) $\nu = 0.82$. Solid and dashed horizontal lines are the average scaled overlap $\langle \delta \rangle / \langle r \rangle$ in the system for the three modes for $w = 1.5$ and $w = 5$, respectively. Note that the y-axis range is different in the two plots. (For interpretation of the references to color in this figure legend, the reader is referred to the web version of the article.)

compression lying between the isotropic and deviatoric datasets. The trend observed in the variation of the scaled pressure and distribution of the average overlaps are consistent with the fact that the isotropic and deviatoric modes are pure modes, while the uniaxial mode is a superposition of isotropic and deviatoric modes (Luding & Perdahcıoğlu, 2011).

Fig. 5(a)–(c) shows the effects of varying polydispersity on the scaled pressure in Eq. (10), where p^* is plotted against volumetric strain $-\varepsilon_v$ for isotropic, uniaxial, and deviatoric deformations. For a single deviatoric deformation the volume fraction is constant along the path and hence the pressure remains practically constant. In this work the data describing deviatoric mode will always refer to the values in the critical state, after large deformation (see Imole et al. (2013a) for more details), unless stated otherwise. In the small strain region, for all deformation modes, the datasets collapse on each other. Only with increasing $-\varepsilon_v$, a small deviation of the simulation data is observed for the isotropic and deviatoric modes, due to the non-linear correction that shows up at large strain in Eq. (10). The analytical expression of the scaled pressure in Eq. (10) fits the simulation data well for all three deformation modes and polydispersity, in agreement with findings in Göncü et al. (2010), Göncü and Luding (2013), and Imole et al. (2013a).

The comparison of Figs. 3 and 4 puts in evidence a very interesting feature in the behavior of pressure. When the contact density νC is scaled out in p^*, the curves collapse irrespective of polydispersity leading to the conclusion that this factor affects the contact network while the deformation mode (and the distance from jamming) influences the evolution of average overlap. The fitted parameters for p^* in Eq. (10) are given in Fig. 6 and Table A1. The parameter p_0 is fairly constant with increasing polydispersity, with p_0 values higher for the isotropic case and uniaxial and deviatoric p_0 being very close. This is in agreement with expectations, as in both uniaxial and deviatoric deformations, anisotropy develops along the path, and the value of the non-dimensional pressure increases for the (pure) isotropic case. The non-linear contribution from γ_p, fluctuates for smaller polydispersity and becomes significant for higher w.

By fitting Eq. (10) for pressure, we can extract the dependence of the jamming volume fraction ν_c on the polydispersity w and the deformation mode, as shown in Fig. 7. The jamming volume fraction increases with increasing polydispersity, showing highest values of ν_c for the isotropic case, with ν_c values for the "mixed" uniaxial mode falling in between the isotropic and deviatoric datasets. This is consistent with findings in Imole et al. (2013a), where $\nu_c^{ISO} > \nu_c^{UNI} > \nu_c^{DEV}$. In this case a similar argument holds as mentioned for p_0, related to the development of anisotropy during the over-compression, that explains the trend of the jamming volume fraction between isotropic, deviatoric and uniaxial. This confirms that the jamming volume fraction is *not an independent (single) value*, i.e. it is not a material parameter, but depends on the deformation history of the packing.

Table 2
Summary of parameters ν_c^0 and ν_c^∞ in Eq. (11) that fit the ν_c vs. w simulation data shown in Fig. 7, for the isotropic, uniaxial, and deviatoric deformation modes.

Mode	ν_c^0	ν_c^∞
ISO	0.6453	0.6710
UNI	0.6394	0.6675
DEV	0.6381	0.6647
Ogarko and Luding (2012)	0.6500	0.6828

A theoretical prediction for the variation in ν_c under isotropic compression of polydisperse hard spheres was presented by Ogarko and Luding (2012), as follows:

$$\nu_c(w) = \nu_c^\infty - (\nu_c^\infty - \nu_c^0)(3w^{-2} - 2w^{-3}), \quad (11)$$

where ν_c^0 and ν_c^∞ are the jamming volume fractions for $w = 1$ and $w \to \infty$, respectively. We apply Eq. (11) to the three deformation modes, and in Fig. 7 we show the prediction for hard spheres together with the ν_c simulation data for the three modes, and the fitting curves, where the parameters ν_c^0 and ν_c^∞ are presented in Table 2. Despite the quantitative disagreement due to the difference between hard and soft spheres, both systems show a very similar trend, the predictions working well for all the three modes. The simulations in Ogarko and Luding (2012), leading to Eq. (11), were carried out by very slow isotropic compression from the low density collisional regime, where the fluctuation velocities were not relaxed as done in this study. The strong kinetic energy fluctuations represent a type of "tapping" that allows the system to relax toward a better packed configurations with larger ν_c. The data in Fig. 7 from Ogarko and Luding (2012) thus represents an upper limit of optimal compaction, which is not reached by e.g.

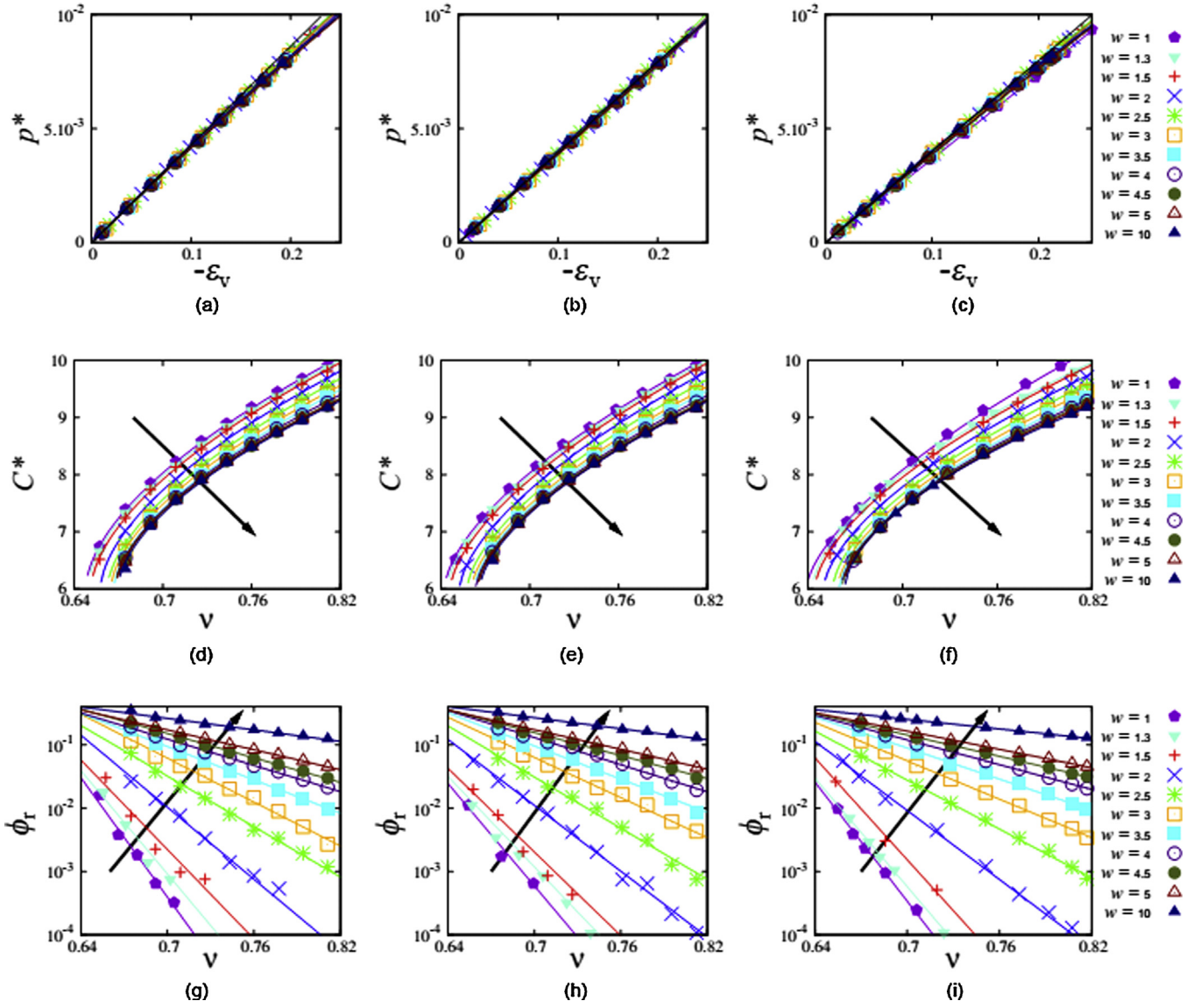

Fig. 5. Effect of polydispersity w on scaled pressure p^*, coordination number C^*, and fraction of rattlers ϕ_r for the three deformation modes, namely isotropic compression (left column), uniaxial compression (middle column), and deviatoric deformation (right column). The solid lines are the fits to the corresponding macroscopic properties using Eqs. (10) and (12) with $C_0 = 6$, $\alpha = 0.60$ for the three modes, and Eq. (13). The arrows indicate the increasing polydispersity. The solid black line in the p^* plot is based on Eq. (10) without the non-linear term. All the fit parameters are presented in Table A1.

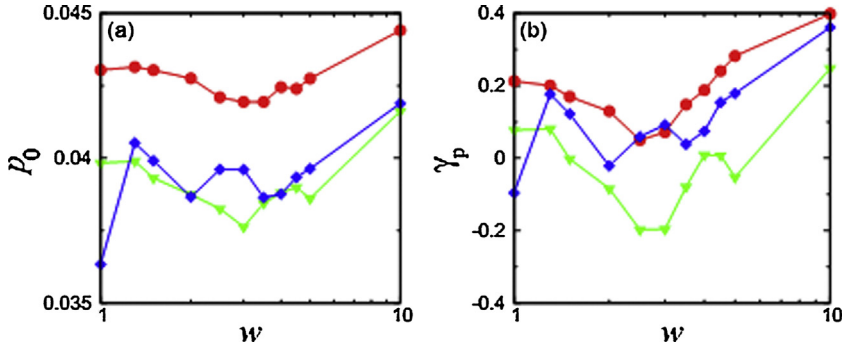

Fig. 6. Comparison of the fitted parameters (a) p_0 and (b) γ_p as a function of polydispersity w with the analytical equations of scaled pressure p^*, i.e., Eq. (10) for the isotropic (●, red), uniaxial (▼, green), and deviatoric (♦, blue) deformation modes. The fitted parameters are presented in Table A1. (For interpretation of the references to color in this figure legend, the reader is referred to the web version of the article.)

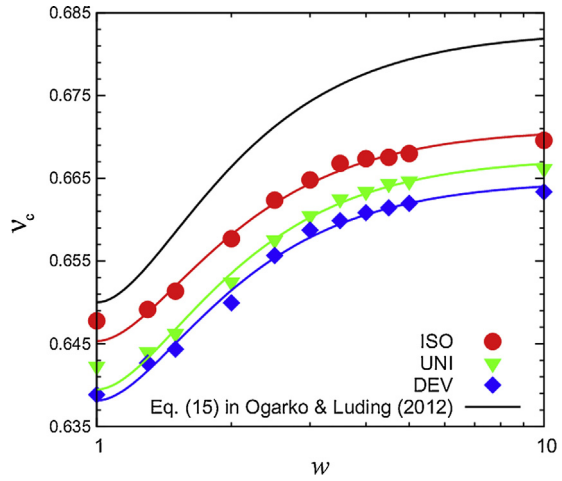

Fig. 7. Variations of jamming volume fraction ν_c with polydispersity w for the deformation modes considered. Corresponding solid lines are the theoretical predictions for different modes using Eq. (11). Note that the fit is applied only to $w > 1.2$, since local crystallization (Ogarko and Luding, 2012; Schröder-Turk et al., 2010) might happen at lower polydispersity causing ν_c values much higher than the disordered, random prediction.

slow over-compression to $\nu_{max} = 0.82$. Eq. (11) can then capture the variation of ν_c with polydispersity, irrespective of the deformation modes, when the fit parameters are properly defined. This interesting feature shows that ν_c acts as a state variable, able to describe the configuration of the assembly and represent its history, as also reflected by the overlaps in Fig. 4.

4.2.2. Coordination number

It has been shown in Göncü et al. (2010) and Imole et al. (2013a) that under isotropic deformation, the corrected coordination number, C^* follows the power law:

$$C^*(\nu) = C_0 + C_1\left(\frac{\nu}{\nu_c} - 1\right)^{\alpha}, \tag{12}$$

where $C_0 = 6$ is the isostatic value in the frictionless case. α and C_1 are fit parameters, while we use ν_c from p^* extrapolation analysis as input value, leading to one less fit parameter for C^*. We observe a very small variation (3%) of α with polydispersity and deformation modes (Imole et al., 2013a) but for simplicity we set it to a fixed value of 0.60 in this work (Peyneau & Roux, 2008). Only C_1 is then the residual free fit parameter.

In Fig. 5(d)–(f), we compare the variation of the corrected coordination number C^* as a function of volume fraction ν during isotropic, uniaxial and deviatoric loadings and show its dependence on polydispersity. The behavior is qualitatively similar for all the three deformation paths: contacts close and the coordination number increases with increasing volume fraction. Moreover, for the three modes, configurations with lower polydispersity result in a higher number of contacts per particle. The data are well fitted by Eq. (12) with the fit parameter C_1 as function of w shown in Fig. 8(a). A systematic decrease in C_1 is observed with increasing polydispersity w. The C_1 values of the "mixed" uniaxial mode lie between the isotropic and deviatoric datasets. Increase in the polydispersity beyond $w = 4.5$ did not lead to a further change of C_1, better clarified by the collapse of the C^* lines (cf. Fig. 5(d)–(f)). This suggests that uniform size polydispersity influences the micromechanics only within a certain limit. For highly polydisperse packings ($w > 5$), the limit is approached because the critical volume fraction ν_c saturates (see Fig. 7). For other size distribution functions, this behavior can be different.

In order to further investigate the behavior of the coordination number C^* we study the distribution of contacts per particle radius fraction. In Fig. 9(a) and (b), we plot the average number of contacts (excluding the rattlers) for a radius range, defined as $C^*(r)$, versus the scaled radius $r_{sc} = (r - r_{min})/(r_{max} - r_{min})$ for $\nu = 0.686$ and $\nu = 0.82$ for the three deformation modes. $C^*(r)$ increases with increasing r_{sc} for all the three modes, that is the number of contacts is larger for bigger particles. This is expected because the bigger particles have larger surface area and thus can be in contact with more particles. A similar argument explains the relation between the particle coordination number $C^*(r)$ and polydispersity: smaller w leads to higher number of contacts for the smallest particles and to a weaker variation of $C^*(r)$ with r_{sc}. The crossover r_{sc} value shifts toward the left for higher volume fractions. As expected, for higher volume fractions, $C^*(r)$ increases faster with r_{sc}, as shown in Fig. 9(b), since more contacts are formed as the volume of the box becomes smaller. Comparing the deformation modes, only very small differences appear, at low volume fraction, $\nu = 0.686$, as shown in Fig. 9(a) and negligible for high volume fraction, $\nu = 0.82$, as seen in Fig. 9(b), in agreement with the argument proposed in Section 4.2.1 for p^*. The average values $\langle C^*(r)\rangle$ for isotropic deformation are smaller, larger for deviatoric, and the "mixed" uniaxial deformation mode lies in between the two (Imole et al., 2013a).

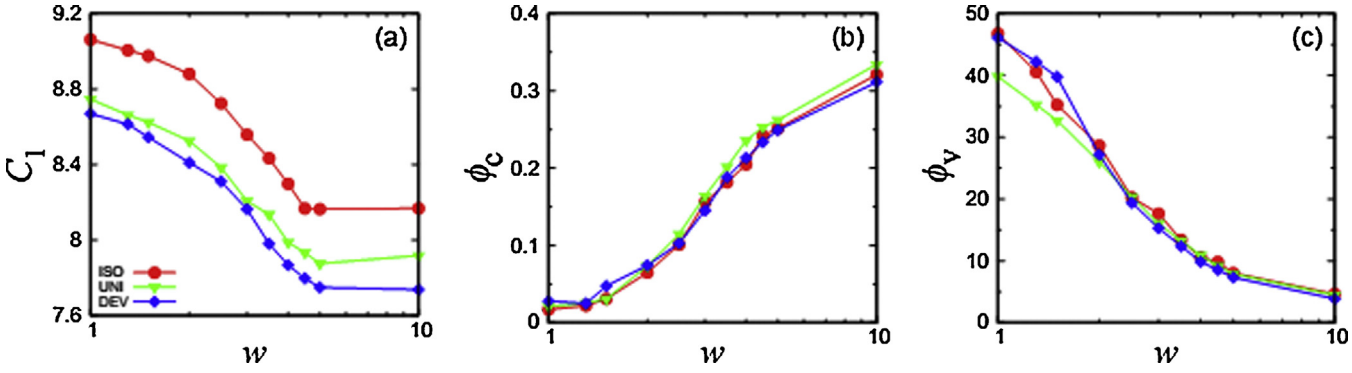

Fig. 8. Comparison of the fit parameters for the analytical equations of coordination number C^* and rattler fraction ϕ_r using Eq. (12) with $C_0 = 6$, $\alpha = 0.60$, and Eq. (13), respectively, for the isotropic (●, red), uniaxial (▼, green), and deviatoric (♦, blue) deformation modes: (a) effect of polydispersity w on the coordination number C^* fit parameter, C_1, and (b) and (c) effect of polydispersity w on rattler fraction ϕ_r fit parameters, ϕ_c and ϕ_v. The fit parameters are presented in Table A1. (For interpretation of the references to color in this figure legend, the reader is referred to the web version of the article.)

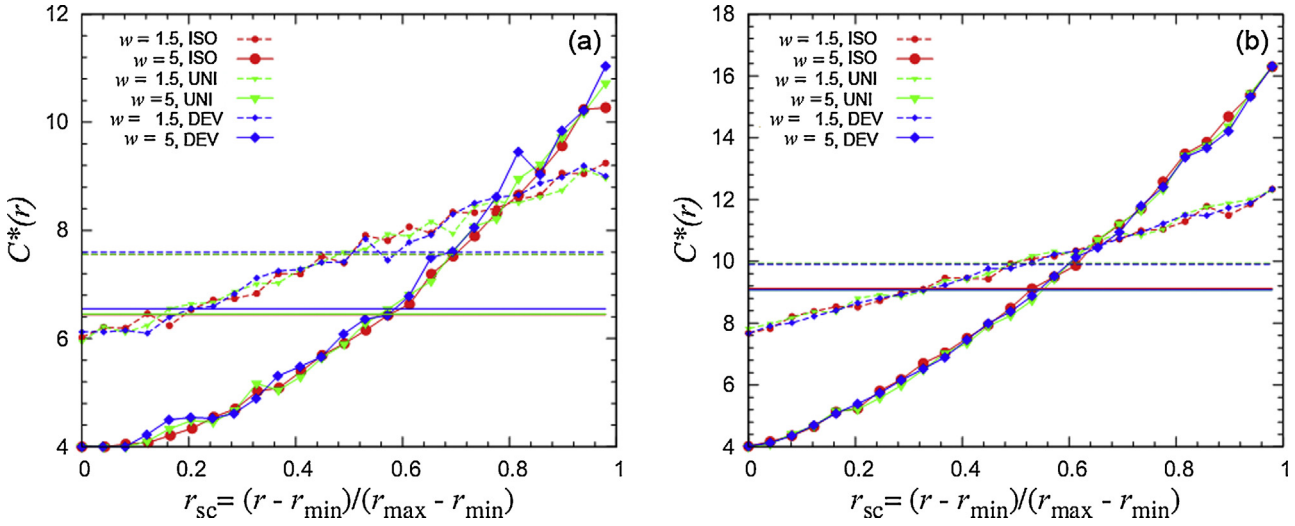

Fig. 9. Average contacts per particle excluding the rattlers $C^*(r)$ for a radius range, plotted against a scaled radius $r_{sc} = (r - r_{min})/(r_{max} - r_{min})$ for the isotropic (●, red), uniaxial (▼, green), and deviatoric (♦, blue) deformation modes. Small symbols represent $w = 1.5$ and big symbols represent $w = 5$. Volume fractions are (a) $\nu = 0.686$ and (b) $\nu = 0.82$. Solid and dashed horizontal lines are the average coordination numbers $\langle C^*(r)\rangle = C^*$ in the system for the three modes, for $w = 1.5$ and $w = 5$ respectively. The horizontal lines represent the average values of the respective $C^*(r)$ plots. The y-axis range is different in the two plots. (For interpretation of the references to color in this figure legend, the reader is referred to the web version of the article.)

4.2.3. Fraction of rattlers

The analytical expression for the fraction of rattlers is proposed (Göncü et al., 2010; Imole et al., 2013a) as

$$\phi_r(\nu) = \phi_c \exp\left[-\phi_v\left(\frac{\nu}{\nu_c} - 1\right)\right], \tag{13}$$

where ϕ_c and ϕ_v are fit parameters, and ν_c is the jamming volume fraction inferred from Eq. (10) for the different deformation modes. We show the effect of polydispersity on the fraction of rattlers under isotropic, uniaxial and deviatoric deformation in Fig. 5(g)–(i), respectively, and the variation of fit parameters with w in Fig. 8(b) and (c) (numerical values are reported in Table A1). A first observation is that the fraction of rattlers decreases exponentially with increasing volume fraction (Imole et al., 2013a) in agreement with Eq. (13). Furthermore, the increase of polydispersity leads to an increase of the fraction of rattlers in the system. This is not surprising, as the volume occupied by finer/smaller particles is smaller in highly polydisperse systems. Contacts of these smaller particles are transient since they have more freedom to move within the system (for this size distribution – not in general). In some cases, they may become "caged" between larger particles without having sufficient (four or more) contacts with their neighbors. This leads to a drop in the coordination number and a (related) increase in the fraction of rattlers.

Also interesting is the variation of the parameters of Eq. (13), ϕ_c and ϕ_v which represent the initial point and the slope, respectively. A systematic increase in ϕ_c with increasing polydispersity is observed in Fig. 8(b), whereas the slope ϕ_v decreases with increasing polydispersity as shown in Fig. 8(c). This indicates that even though the fraction of rattlers in highly polydisperse systems is higher, the rate at which rattlers are lost in these systems during compression decreases with w. This is again related with the "cage" argument, as very small particles are caged by big particles and need a high compression degree to gain new contacts as compared to medium sized particles (see Fig. 9(a) and (b)). Interestingly, both parameters ϕ_c and ϕ_v, as presented in Fig. 8, are seemingly unaffected by the deformation mode, stating that the history of the sample can be fully represented by ϕ_c, when the fraction of rattlers is analyzed.

Finally, we plot in Fig. 10 the variation of the isotropic fabric $F_v = g_3 \nu C$ versus volume fraction during isotropic compression. F_v increases with volume fraction ν and polydispersity w and shows a trend with respect to w opposite to that of the corrected coordination number C^* shown in Fig. 5(d)–(f). This can be explained by observing the rattlers: when particles with less than four contacts are included in the calculation of C, the value of F_v grows with increasing w and ν. For both polydispersities shown, near the jamming volume fraction, deviatoric deformation has the highest F_v, isotropic deformation has the lowest and the "mixed" uniaxial mode is in between the two, as shown in the inset of Fig. 10. This variation disappears for large volume fractions. However, the differences between the three modes for F_v are smaller compared to

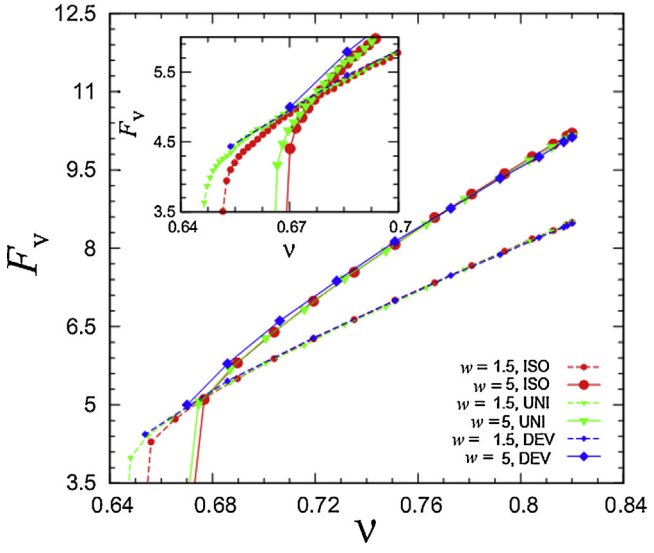

Fig. 10. Variations of isotropic fabric F_v with volume fraction ν for the isotropic (●, red), uniaxial (▼, green), and deviatoric (♦, blue) deformation modes. As shown in the legend, small symbols represent $w = 1.5$ and big symbols represent $w = 5$. Inset is the zoomed-in area near the jamming volume fractions. (For interpretation of the references to color in this figure legend, the reader is referred to the web version of the article.)

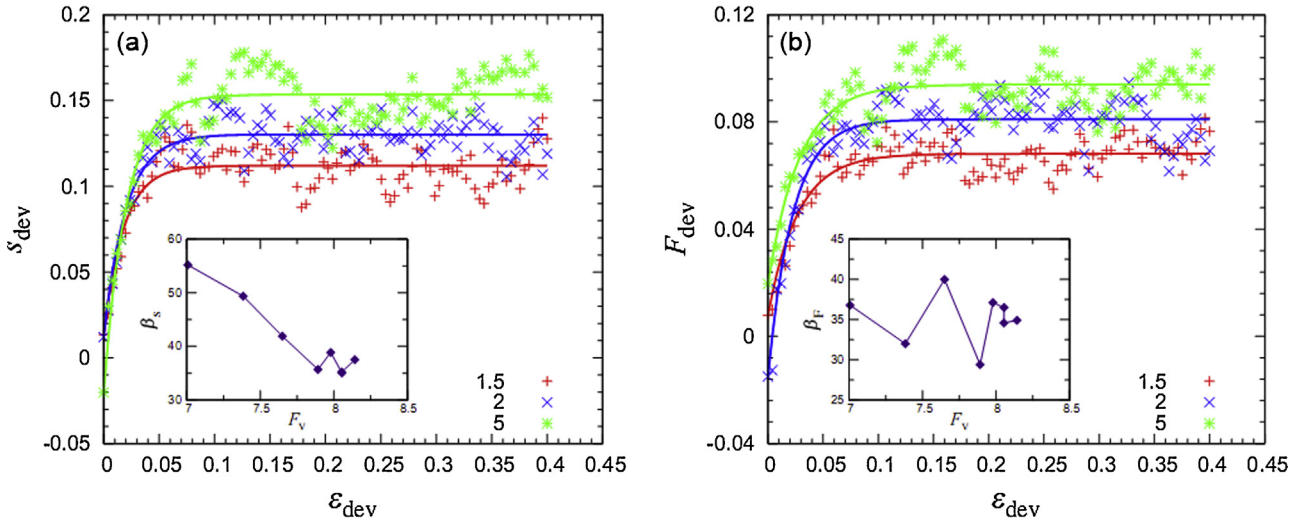

Fig. 11. (a) Deviatoric stress ratio $s_{dev} = \sigma_{dev}/P$ plotted against deviatoric strain from the deviatoric (volume conserving) mode for three polydispersities $w = 1.5$, 2, and 5 as shown in the legend for volume fraction $\nu = 0.75$; (b) deviatoric fabric F_{dev} plotted against deviatoric strain for the same cases as in (a). The data points are simulation results while the solid lines through them are fits to the data using Eq. (16) for (a) and Eq. (17) for (b). The corresponding insets show the behavior of growth rates β_s and β_F with isotropic fabric F_v for different w.

the isotropic part of stress p, as it is related to small differences in the average contact number per particle (Fig. 9(a) and (b)).

4.3. Effect of polydispersity on deviatoric quantities

In this section, we present the effects of polydispersity on the evolution of deviatoric stress and deviatoric fabric along uniaxial and deviatoric deformation paths. The deviatoric stress is a macroscopic property which quantifies the stress anisotropy (Imole et al., 2013a), while the deviatoric fabric is a microscopic property related to the orientation of the contact network. Here, we focus on the simulation results for the uniaxial and deviatoric deformation modes since the deviatoric quantities only fluctuate around zero for the isotropic mode. Later in Section 5, we will use the information obtained from the above mentioned quantities to calibrate a constitutive model. As a result, we will test the predictive ability of the model on an independent uniaxial compression test.

4.3.1. Deviatoric stress

In Fig. 11(a), we plot the deviatoric stress ratio ($s_{dev} = \sigma_{dev}/P$) as a function of deviatoric strain ε_{dev} during deviatoric deformation for packings with three different polydispersities. The volume fraction ν is 0.751 in all cases, and stays constant during the numerical experiments. The deviatoric stress grows initially with rate β_s from random initial values (a small random initial anisotropy is present in each sample) until an asymptote, s_{dev}^{max} at steady state is reached, where it remains fairly constant (Cui & O'Sullivan, 2006; Imole et al., 2013a; Kumar et al., 2013; Krijgsman & Luding, 2013; Luding, 2004). The steady state value increases with polydispersity with highly fluctuating values varying in the range of 0.11 ± 0.02, 0.12 ± 0.03 and 0.15 ± 0.035 for $w = 1.5$, 2, and 5, respectively. Surprisingly, while the deviatoric stress σ_{dev} is practically unaffected by w, the pressure P decreases with increasing polydispersity (see Fig. 3), leading to the dependence of the ratio σ_{dev}/P on w as observed. On the other hand, the slope β_s, proportional to the shear stiffness (scaled by pressure) of the initial isotropic configurations, is a function of the isotropic fabric F_v, as shown in the inset of Fig. 11(a). The relation between isotropic fabric and polydispersity, extensively discussed in Göncü et al. (2010) and reported in Fig. 10, makes β_s a decreasing function of w.

Furthermore, in Fig. 12(a) we plot the deviatoric stress as a function of deviatoric strain during uniaxial compression, for packings with different polydispersity $w = 1.5$, 2, and 5. The uniaxial test starts from initial volume fraction $\nu_i = 0.72$ (the same value used for the previous deviatoric simulations), and reaches the maximum volume fraction $\nu_{max} = 0.82$. As for the deviatoric simulations, higher polydispersity also leads to higher s_{dev}^{max} at steady state for the uniaxial deformations. The same argument about the dependence of pressure on polydispersity holds and explains the behavior in Fig. 12(a). We observe larger fluctuations for the uniaxial deformation mode as compared to the deviatoric deformation, with averages and errors $s_{dev}^{max} \approx 0.10 \pm 0.025$, 0.11 ± 0.035 and 0.15 ± 0.04 for $w = 1.5$, 2, and 5, respectively. We relate the increasing fluctuations to the non-conserved volume (Imole et al., 2013a) and more "violent" rearrangements. Note that different sign conventions are used in Eq. (6) to calculate the deviatoric stress for deviatoric and uniaxial simulations, since the definition of the sign function Fsgn depends on the deformation mode, as discussed in Section 2, i.e. the strain eigen-system. The sign function for uniaxial compression (negative strain components versus positive stress and fabric) is

$$\mathrm{Fsgn}(\mathbf{Q}) = \mathrm{sgn}(Q_{zz} - 0.5(Q_{xx} + Q_{yy})),$$

where the z-wall is moving and the x- and y-walls are not. For deviatoric deformation

$$\mathrm{Fsgn}(\mathbf{Q}) = \mathrm{sgn}(Q_{yy} - Q_{xx}),$$

with x-wall expanding, y-wall compressing and a non-mobile z-wall. The sign convention explains the different initial values associated to the same initial packings in Figs. 11(a) and 12(a).

4.3.2. Effect on deviatoric fabric

The variation of the deviatoric fabric F_{dev} as a function of the deviatoric strain ε_{dev} is shown in Fig. 11(b) for the same deviatoric simulations as above. F_{dev} builds up from different random (small) initial values with rate β_F to different saturation values F_{dev}^{max}. Interestingly, the slope β_F seems to be constant (besides large fluctuations), irrespective of different polydispersity of the initial configurations. This is surprising, as the initial samples have different contact network densities F_v, due to polydispersity, and leads

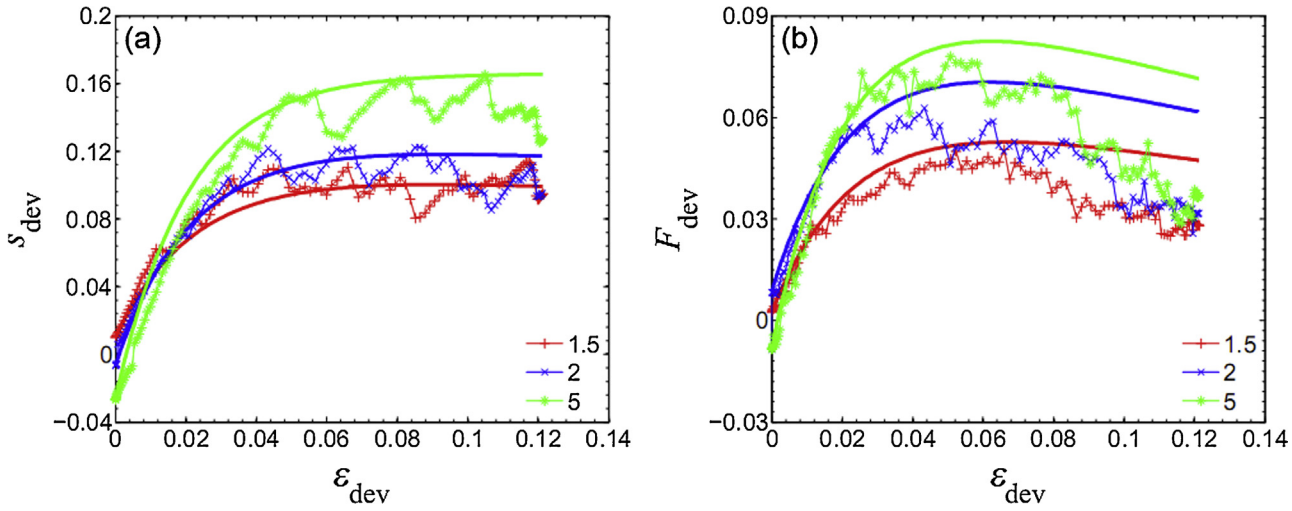

Fig. 12. (a) Deviatoric stress ratio $s_{dev} = \sigma_{dev}/P$ plotted against deviatoric strain from the uniaxial mode for three polydispersities $w = 1.5$, 2, and 5 as shown in the legend; (b) deviatoric fabric F_{dev} plotted against deviatoric strain for the same cases as in (a). The data points are the simulation results while the solid lines through them represent a prediction to the data using Eq. (16) for (a) and Eq. (17) for (b). The starting volume fraction $\nu_i = 0.72$ and the maximum volume fraction $\nu = 0.82$ for all the cases of polydispersity.

to the interesting conclusion that the incremental response of deviatoric fabric only depends on F_{dev} and volume fraction as state variables, while the role of the isotropic contact network is negligible. The critical value F_{dev}^{max} shows a different trend from β_F, but similar to s_{dev}^{max} as it increases with polydispersity w. This is reasonable, when we think of the kinematics at small scale, i.e. particles with a large difference in size have more freedom to rearrange and modify the contact network during compression. The behavior of s_{dev}^{max} is consistent with the decrease of C^* in Fig. 5(e)–(f), as a lower coordination number is usually associated with a higher anisotropy (La Ragione & Magnanimo, 2012).

In order to further investigate the anisotropic behavior of the material, we study the deviatoric fabric $F_{dev}(r)$ per particle radius for the volume conserving deviatoric tests focusing on the large shear strain configurations, i.e. $\varepsilon_{dev} = 0.40$. We focus only on the contact orientation and cancel the influence of the particle radius, by slightly modifying Eq. (3) such that this quantity stays bin independent. For each radius r, we calculate

$$\mathbf{F}(r) = \frac{1}{V}\frac{\sum V^P}{\sum V_r}\sum_{P\in V_r} V^P \sum_{c\in P} \mathbf{n}^c \otimes \mathbf{n}^c, \tag{14}$$

where the value of fabric is scaled by the ratio $\sum V^P/\sum V_r$ between the total volume of the particles having radius r and the total volume of the particles. Please notice that Eq. (14) coincides with Eq. (3) when all the radii are considered and $\sum V_r = \sum V^P$. In Fig. 13(a) and (b), we plot the deviatoric part of fabric, $F_{dev}(r)$ versus the scaled radius $r_{sc} = (r - r_{min})/(r_{max} - r_{min})$ for $\nu = 0.686$ and $\nu = 0.82$. $F_{dev}(r)$ increases with increasing r_{sc}, meaning that the bigger particles form a sub-network, whose orientation follows the applied shear strain. These are the particles that belong to the force chains (Radjaï et al., 1999) and carry the majority of the applied load. On the other hand, $F_{dev}(r)$ is small for small r_{sc}, as the small particles arrange randomly, i.e. isotropically and are "caged" in the voids among the bigger particles, as already mentioned in Section 4.2.2. Large fluctuations do not allow to clearly read how the behavior of $F_{dev}(r)$ vs r_{sc} depends on polydispersity w.

The variation of the deviatoric fabric under uniaxial deformation is presented in Fig. 12(b) for different polydispersities. In a similar fashion to the deviatoric stress ratio, F_{dev} builds up from different (random, but small) initial values and reaches different maxima for different polydispersities, with $w = 5$ showing the highest peak, while the slope β_F stays unaffected by w. For larger strain, the structural anisotropy decreases rapidly toward zero (data not shown). This indicates that more new contacts are created in the axial direction compared to the perpendicular isotropic plane at the beginning of the loading path while at higher deviatoric strain, the fabric behaves in an opposite fashion as new contacts are created in the horizontal direction rather then in the vertical one, where most available neighbors already have come into contact. The "softening" in deviatoric fabric does not correspond to any decrease in deviatoric stress that grows monotonically until saturation is reached (see Fig. 12(a)). The origin of this interesting feature associated with uniaxial simulation, where stress and fabric show non-colinearity, and the strain eigen-system is prescribed by the wall motion, will be presented elsewhere (Imole, Wojtkowski, Kumar, Magnanimo, & Luding, 2013b).

5. Calibration of the continuum model and prediction

In this section, we will present the microscopic simulation results with a short review of an anisotropy continuum model as introduced in Luding and Perdahcıoğlu (2011). We will calibrate the free parameters in the model as function of polydispersity w and volume fraction ν, using the isotropic and purely deviatoric deformation experiments. Finally, using the model, a prediction of an independent test, i.e. the uniaxial deformation mode, will be presented.

5.1. Reduced theoretical model

Most standard constitutive models with wide application fields, like elasticity, elasto-plasticity, or fluid/gas flow models of various kinds, were applied also to granular flows, sometimes with success but typically only in a very limited range of parameters and flow conditions (for overviews see Bauer, Huang, & Wu, 2004; Einav, 2012; Göncü & Luding, 2013; Imole et al., 2013b; Jiang & Liu, 2007; Luding & Perdahcıoğlu, 2011; MiDi, 2004; Tejchman & Wu, 2007 and references therein). While most of these theories can be and some have been extended to accommodate anisotropy of the microstructure, only very few models account for an independent

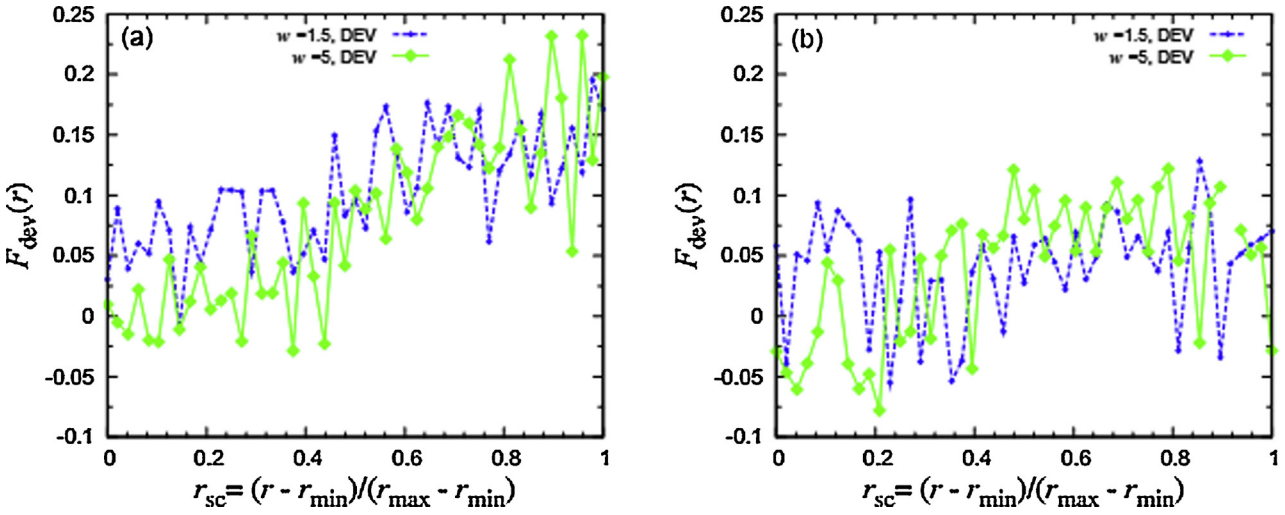

Fig. 13. Deviatoric fabric per particle radius fraction $F_{dev}(r)$, plotted against a scaled radius $r_{sc} = (r - r_{min})/(r_{max} - r_{min})$ for the deviatoric deformation mode, after large shear strain $\varepsilon_{dev} = 0.40 = 0.40$. Small (blue) symbols represent $w = 1.5$ and big (green) symbols represent $w = 5$. Volume fractions are (a) $\nu = 0.686$ and (b) $\nu = 0.82$. (For interpretation of the references to color in this figure legend, the reader is referred to the web version of the article.)

evolution of the microstructure (e.g. Goddard, 2006; Luding & Perdahcıoğlu, 2011; Sun & Sundaresan, 2011).

We use the constitutive model, as proposed in Luding and Perdahcıoğlu (2011), generalized for a D-dimensional system:

$$\begin{aligned} \delta P &= DB\delta\varepsilon_v + AS\delta\varepsilon_{dev}, \\ \delta\sigma_{dev} &= DA\delta\varepsilon_v + G^{oct}S\delta\varepsilon_{dev}, \\ \delta A &= \beta_A \text{sign}(\delta\varepsilon_{dev})(A^{max} - A)\delta\varepsilon_{dev}. \end{aligned} \tag{15}$$

The model involves three moduli, namely, the classical bulk modulus B (Göncü et al., 2010), the octahedral shear modulus G^{oct}, and the "anisotropy modulus" A. Due to the modulus A, the model provides a cross coupling between the two types of stress and strain in the model, namely the hydrostatic and the shear (deviatoric) stresses react to both isotropic and deviatoric strains. $S = (1 - s_{dev}/s_{dev}^{max})$ is an abbreviation for the stress isotropy with the stress ratio s_{dev} already introduced in Section 4.3. The parameter s_{dev}^{max} resembles the macroscopic friction (depending on our definition, $s_{dev} = 3q = 3\sin\varphi$, where q is the shear stress ratio and φ is the internal friction angle as in Azéma, Radjaï, and Saussine (2009) and others, while β_s is the growth rate of s_{dev}. The parameter A^{max} in the evolution equation of A represents the maximum anisotropy that can be reached at saturation, and $\beta_A = \beta_F$ determines how fast the asymptote is reached (growth rate) when a material is subjected to deviatoric strain ε_{dev} (Imole et al., 2013a). Both A^{max} and β_A are model parameters and can be extracted by fitting the macroscopic simulation results. In a nutshell, the anisotropy model is based on the basic postulate that an independent evolution of stress and structure is possible and the macroscopic modulus A accounts for the deviatoric deformation history, being proportional to the microscopic rank-two deviatoric fabric F_{dev}. More detailed explanations about the constitutive model and its parameters can be found (in Imole et al., 2013a; Luding & Perdahcıoğlu, 2011; Magnanimo & Luding, 2011; Krijgsman & Luding, 2013).

The reduced model, with some simplifying assumptions as introduced in Imole et al. (2013a) and Luding (2004, 2005b), reduces to only two independent evolution equations for the deviatoric stress ratio s_{dev}, and the deviatoric fabric F_{dev}, where the former is given by:

$$s_{dev} = s_{dev}^{max} - (s_{dev}^{max} - s_{dev}^{0})e^{-\beta_s\varepsilon_{dev}}, \tag{16}$$

where s_{dev}^{0} and s_{dev}^{max} represent the initial and maximum values of s_{dev} and β_s is its growth rate. Similarly, the deviatoric fabric is approximated by:

$$F_{dev} = F_{dev}^{max} - (F_{dev}^{max} - F_{dev}^{0})e^{-\beta_F\varepsilon_{dev}}, \tag{17}$$

where F_{dev}^{0} and F_{dev}^{max} represent the initial and maximum (saturation) values of the deviatoric fabric, and β_F is its rate of change.

5.2. Calibration for polydisperse samples

In the following, we use these two equations as empirical fit functions, since they are special cases of the complete constitutive model with anisotropy, to deduce the model parameters as functions of volume fraction ν from various volume-conserving deviatoric simulations (Imole et al., 2013a). In particular, the influence of polydispersity w on the fitting parameters is studied. As an example, the deviatoric data for $w = 1.5$, 2, and 5 are fitted using Eqs. (16) and (17) and the four parameters s_{dev}^{max}, β_s, F_{dev}^{max}, and β_F are extracted. The procedure is applied to the full set of polydisperse packings with many different ν (not shown).

Fig. 14(a) and (b) shows respectively the variation of s_{dev}^{max} and F_{dev}^{max} with ν, for different w. Both s_{dev}^{max} and F_{dev}^{max} decrease with increasing volume fraction ν and approach a finite limit for large volume fractions. This is because for higher volume fractions, the motion of spheres is more constrained by more contacts and hence the anisotropy developed during the deformation becomes smaller. Moreover, with increasing polydispersity, the asymptotic values of s_{dev}^{max} and F_{dev}^{max} increase, as explained in detail in Section 4.3.

Fig. 15(a) and (b) shows respectively the variations of β_s and β_F with ν relative to the jamming volume fraction, i.e. the scaled volume fraction $\nu/\nu_c - 1$, for different w from the same deviatoric simulations as above. A decreasing trend is seen for β_s versus $\nu/\nu_c - 1$, with larger scattering as compared to s_{dev}^{max}. With increasing polydispersity, the variation of β_s with polydispersity w reduces (this can be seen by looking at the inset in Fig. 11(a) since F_v in that dataset depends only on polydispersity), so we neglect this variation in this work. A similar decreasing trend in β_F with $\nu/\nu_c - 1$ is seen, while, besides fluctuations, β_F is less dependent on w (see inset in Fig. 11(b)). In Figs. 14 and 15, we also report the values of the four parameters for the monodisperse packing, $w = 1$. We note that when β_s and β_F are plotted in Fig. 15(a) and (b), the data for $w = 1$ show anomalously large values. This is probably

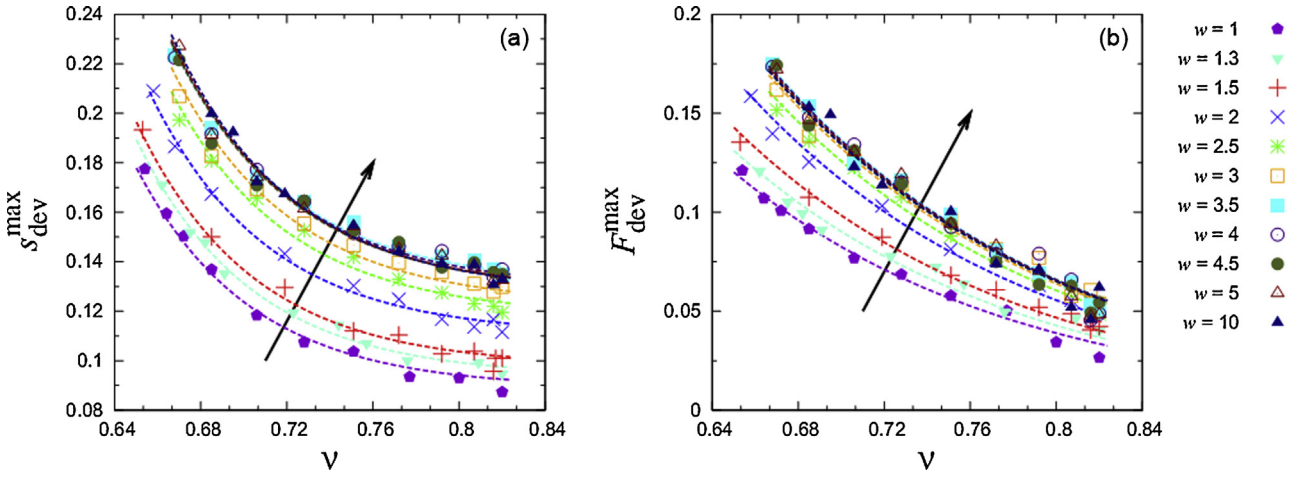

Fig. 14. Comparison of variations of parameters for normalized deviatoric stress s_{dev} and deviatoric fabric F_{dev} with polydispersity w for the deviatoric deformation mode: (a) the maximum normalized deviatoric stress s_{dev}^{max} plotted against volume fraction ν and (b) the maximum deviatoric fabric F_{dev}^{max} plotted against volume fraction ν. The arrow indicates the increasing w. The corresponding dashed lines are the fit using Eq. (18).

due to partial, local crystallization (Schröder-Turk et al., 2010 and references therein) present in the monodisperse case.

A clear difference between the fit parameters of deviatoric stress and deviatoric fabric, namely the steady values s_{dev}^{max}, F_{dev}^{max} (Fig. 14(a) and (b)), and the growth rates β_s and β_F (Fig. 15(a) and (b)) can be seen. This confirms that stress and fabric indeed evolve independently with deviatoric strain (Imole et al., 2013a; La Ragione & Magnanimo, 2012), as is the basic postulate for the anisotropy constitutive model.

We propose a generalized analytical relation to fit the stress parameters s_{dev}^{max}, β_s and the fabric parameters F_{dev}^{max}, β_F, obtained from different volume-conserving deviatoric simulations. Their

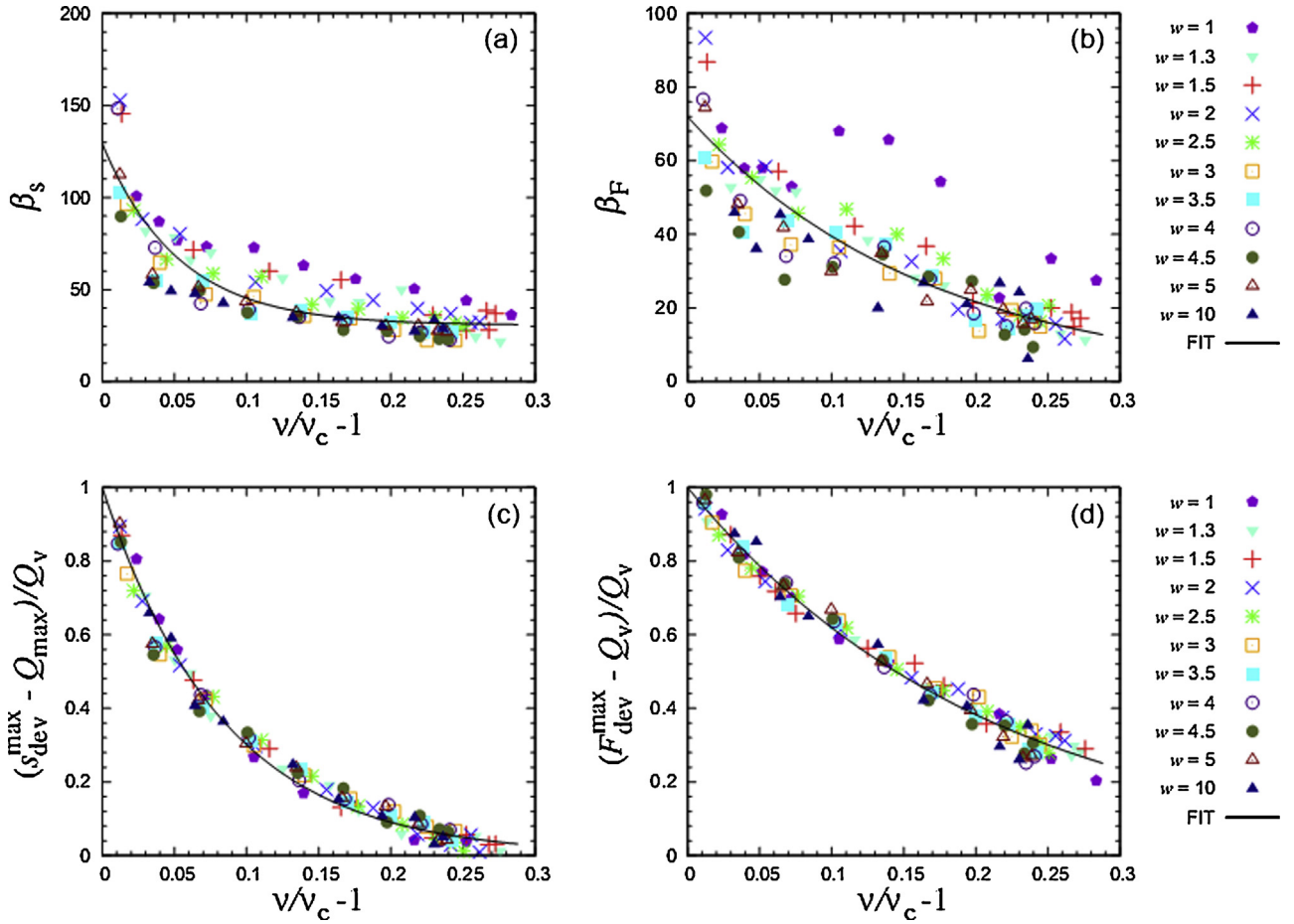

Fig. 15. The growth rates (a) β_s of s_{dev} and (b) β_F of F_{dev} plotted against scaled volume fraction, $(\nu/\nu_c - 1)$. Scaled (c) s_{dev}^{max} and (d) F_{dev}^{max} with components Q_{max} and Q_v (see Table 3) plotted against scaled volume fraction, $(\nu/\nu_c - 1)$. The corresponding solid lines are the scaled parameters using Eq. (18) with data taken from Table 3.

Table 3
Fitted coefficients for the fitting parameters in Eqs. (16) and (17), using Eq. (18)) with ν_c (w) extracted from Table A1, by fitting the results obtained from various volume-conserving deviatoric deformation simulations with different w.

w	ν_c	s_{dev}^{max}			F_{dev}^{max}		β_s			β_F	
		Q_{max}	Q_v	α	Q_v	α	Q_{max}	Q_v	α	Q_v	α
1.0	0.6389	0.0888			0.1308						
1.3	0.6427	0.0935			0.1386						
1.5	0.6444	0.0976			0.1491						
2.0	0.6500	0.1106			0.1684						
2.5	0.6557	0.1164			0.1741						
3.0	0.6587	0.1226	0.11	12	0.1789	4.8	31	116	22	72	6
3.5	0.6599	0.1303			0.1830						
4.0	0.6609	0.1292			0.1810						
4.5	0.6614	0.1278			0.1777						
5.0	0.6620	0.1279			0.1782						
10.0	0.6634	0.1273			0.1751						

dependence on volume fraction ν (see Imole et al. (2013a), for $w = 3$), is well described by the general relation:

$$Q = Q_{max}(w) + Q_v(w) \exp\left(-\alpha(w)\left(\frac{\nu}{\nu_c(w)} - 1\right)\right), \tag{18}$$

where $Q_{max}(w)$, $Q_v(w)$ and $\alpha(w)$ are the fitting parameters depending on polydispersity w, with the values presented in Table 3, ν is the volume fraction and $\nu_c(w)$ is the jamming volume fraction for the deviatoric deformation mode depending on w (see Fig. 7). For all four model parameters, $Q_{max}(w)$ is the limit value for large volume fraction, $Q_c = Q_{max}(w) + Q_v(w)$ represents the limit at $\nu \to \nu_c(w)$, and $\alpha(w)$ is the rate of variation (decay) with the volume fraction.

Here we study and discuss the four cases separately. For s_{dev}^{max}, from Fig. 14(a), we observe a systematic variation of Q_{max} with w and the curves are parallel. Hence Q_v and α can be considered independent of w. Scaling the curves in s_{dev}^{max} by $(s_{dev}^{max} - Q_{max}(w))/Q_v$, leads to a collapse of the data, as shown in Fig. 15(c). For β_s, in this work, we neglect its weak variation with w and assume constant values for the fitting parameters Q_{max}, Q_v and α. When looking at the structural anisotropy, since both F_{dev}^{max} and β_F tend to 0 as the volume fraction increases, we assume, for consistency in the simulation data, that $Q_{max} = 0$ in their fitting functions. We observe in Fig. 14(b) that the variation of Q_v with w is systematic for F_{dev}^{max}. When F_{dev}^{max} is scaled by $(F_{dev}^{max} - Q_v)/Q_v$, the data collapse as shown in Fig. 15(d). Since the curves have the same trend α is set constant, independent of w. As shown in the inset of Fig. 11(b), β_F is independent of the initial configuration, that is w, and we set constant Q_v and α in this case.

Interestingly, we can reduce Eq. (18) in a very compact form by expressing the two w-dependent parameters $Q_{max}(w)$ for s_{dev}^{max}, and $Q_v(w)$ for F_{dev}^{max} as functions only of $\nu_c = \nu_c(w)$:

$$\begin{aligned} s_{dev}^{max}(\nu, w) &= Q_{max}(\nu_c) + Q_v \exp(-\alpha(\nu/\nu_c - 1)) \\ \beta_s(\nu, w) &= Q_{max} + Q_v \exp(-\alpha(\nu/\nu_c - 1)) \\ F_{dev}^{max}(\nu, w) &= Q_v(\nu_c) \exp(-\alpha(\nu/\nu_c - 1)) \\ \beta_F(\nu, w) &= Q_v \exp(-\alpha(\nu/\nu_c - 1)) \end{aligned} \tag{19}$$

with $Q_{max} = -1 + 1.7\nu_c$ for s_{dev}^{max} and $Q_v = -0.9 + 1.6\nu_c$ for F_{dev}^{max}. Using these two equations, every term in Eq. (19) can be expressed as either constant, or as function of ν_c, that becomes a unique state variable able to describe the history of the material due to its deformation mode. Using these equations, together with ν_c data from Table 2, and constant parameters from Table 3, we can represent the variations of the model parameters s_{dev}^{max}, β_s, F_{dev}^{max} and β_F with volume fraction ν and polydispersity w, and use them to predict the behavior during uniaxial deformation.

5.3. Prediction of uniaxial deformation for polydisperse samples

Fig. 12(a) shows the deviatoric stress ratio s_{dev} against deviatoric strain ε_{dev} for uniaxial deformations, compared with the predictions of Eq. (16) with coefficients $s_{dev}^{max}(\nu, w)$ and $\beta_s(\nu, w)$ taken from Eq. (19). The proposed model, although in its simplified version, captures the behavior of the material qualitatively, s_{dev} increasing exponentially to a maximum value and then decreasing due to the volume fraction and polydispersity dependence of the parameters.

Fig. 12(b) shows the evolution of deviatoric fabric, F_{dev}, with deviatoric strain, ε_{dev}, for uniaxial deformations – as above – together with the predictions of Eq. (17), with parameters taken from Eq. (19). The model is still able to qualitatively describe the behavior of the deviatoric fabric, but with order of 30% overprediction for large strain. Note that the softening present in some of the deviatoric DEM data, is on purpose not plugged into the model as a constraint, which renders the weak softening present in some of the uniaxial data as a valuable prediction of the model. For better understanding, the complete coupled model needs to be used and possibly improved, as will be presented elsewhere.

6. Summary and outlook

We use the discrete element method to investigate the behavior of three-dimensional frictionless granular assemblies characterized by different polydispersities and subjected to various deformation paths. In particular, isotropic loading/unloading, deviatoric (pure) shear, and uniaxial compression are studied.

The main goal is to analyze and understand the reciprocal influence of polydispersity and deformation history on the response of the material, where the structural/bulk effects are highlighted by using the simplest linear visco-elastic contact model. The evolution of the scaled pressure as a function of volumetric strain (relative to the jamming volume fraction ν_c) is well described by an analytical (linear, to very good approximation) scaling equation, see Eq. (10). This shows that the isotropic fabric is proportional to the isotropic stress provided proper parameters, slightly depending on the deformation mode, are included. Notably, only the jamming volume fraction, among the fit parameters for the pressure, describes the role of both polydispersity and deformation history on the material behavior. As reported earlier in Imole et al. (2013a), the isotropic jamming volume fraction ν_c is not a constant value for a particular material and system configuration but is strongly dependent on the deformation mode and history of the packing. Moreover, ν_c increases with polydispersity, following the behavior described in Ogarko and Luding (2012), with the isotropic and deviatoric tests giving the highest and lowest values, respectively, while the uniaxial dataset lies in between. On the

contrary, the shear jamming volume fraction, slightly below the isotropic jamming volume fraction, has been confirmed as a lower limit value in recent studies, independent of the deformation path (Bi, Zhang, Chakraborty, & Behringer, 2011). The detailed simulations by Ogarko and Luding (2012), using hard instead of soft spheres, represent lower or upper bounds to ν_c if they are carried out extremely fast or slow, respectively. However, the relation between these distinct results has to be further studied.

The behavior of polydisperse systems has been predicted by Ogarko and Luding (2012), to depend on the moments of their size distribution, provided the rattlers are excluded. For larger w, the moments (scaled by $\langle r \rangle$) do not change much above $w \approx 3$–4, which explains the saturation of many quantities – for the uniform size distribution used in this work.

When the micromechanics is analyzed, the coordination number decreases with polydispersity, while the fraction of rattlers displays an opposite trend, increasing with w. In these cases, the evolution of the state variables can be predicted using the evolution equations from Göncü et al. (2010), with parameters depending on the polydispersity of the packing, while the laws for the critical volume fraction $\nu_c(w)$ as extrapolated from the pressure behavior are used. Interestingly, the free fit parameters are not affected by the deformation modes in the case of the micromechanical quantities, that is, they are fully described by the evolution of the critical volume fraction, acting as history variable for the sample.

During deviatoric and uniaxial deformations, both deviatoric stress ratio and deviatoric fabric evolve with the deviatoric strain, reaching saturation values that increase with polydispersity. The initial growth rate of stress, β_s, depends on polydispersity due to the relation between the shear stiffness of isotropic samples and the volumetric fabric $F_v(w)$. On the other hand the growth rate of deviatoric fabric β_F is fairly independent of polydispersity (besides fluctuations), suggesting that the incremental response of the granular deviatoric fabric is not directly related to its isotropic state F_v.

The DEM data of isotropic compression (Göncü et al., 2010) and volume-conserving deviatoric tests are used to calibrate a simple constitutive model that involves anisotropy as proposed in 2D by Luding and Perdahcıoğlu (2011) and Magnanimo and Luding (2011). The four parameters that characterize the model, s_{dev}^{max}, β_s, F_{dev}^{max}, and β_F are expressed as functions of volume fraction and polydispersity. They show a very similar behavior, decreasing exponentially from a maximum value at the jamming volume fraction to a saturation minimum. Also in this case, where only two parameters are dependent on w and thus $\nu_c(w)$, the dependence on polydispersity can be fully described through the established variation of the jamming volume fraction $\nu_c(w)$ with w.

As final step, the constitutive model calibrated on isotropic and deviatoric data is used to predict both stress and fabric evolution under uniaxial deformation, with very good qualitative success and within 70–80% quantitative agreement. The successful prediction of the uniaxial test suggests promising perspectives for future research. The basic qualitative features are captured by the model, even though it is used in a very idealized and short form, e.g. with a single anisotropy modulus. In the future, the coupled equations have to be solved and additional formulations/terms that relate anisotropy (possibly a second anisotropy modulus) with the deviatoric fabric will also be added. Moreover, it would be interesting to look deeper into different distributions of polydispersity like constant volume fraction, or log-normal distributions.

Acknowledgements

Helpful discussions with V. Ogarko, M. B. Wojtkowski, A. Singh, F. Göncü, and J. Ooi are gratefully acknowledged. The authors also appreciate the work of the final proofreaders in improving the quality of the manuscript. This work is financially supported by the European Union funded Marie Curie Initial Training Network, FP7 (ITN-238577), see http://www.pardem.eu/for more information.

Appendix A.

Dependence of the model parameters for pressure, coordination number and fraction of rattlers on the width w of the size distribution.

Table A1
Summary of parameters used in Eqs. (10) and (12) with $C_0 = 6$, $\alpha = 0.60$ for the three modes, and Eq. (13) as function of polydispersity w.

w	ν_c	p_0	γ_p	C_1	ϕ_c	ϕ_v
ISO						
1.0	0.6478	0.0430	0.2131	9.0622	0.0171	46.7722
1.3	0.6491	0.0432	0.2010	9.0053	0.0220	40.5552
1.5	0.6514	0.0430	0.1698	8.9759	0.0309	35.2452
2.0	0.6577	0.0428	0.1299	8.8795	0.0650	28.6337
2.5	0.6624	0.0421	0.0499	8.7233	0.1010	20.2312
3.0	0.6648	0.0419	0.0720	8.5585	0.1559	17.6338
3.5	0.6668	0.0419	0.1481	8.4082	0.1818	13.4036
4.0	0.6674	0.0425	0.1882	8.2977	0.2049	10.5633
4.5	0.6675	0.0424	0.2409	8.1672	0.2417	9.8332
5.0	0.6680	0.0428	0.2825	8.1636	0.2513	8.0380
10.0	0.6696	0.0444	0.3992	8.1674	0.3210	4.6514
UNI						
1.0	0.6423	0.0398	0.0776	8.7464	0.0212	39.8092
1.3	0.6440	0.0399	0.0808	8.6618	0.0254	35.2456
1.5	0.6463	0.0393	−0.0025	8.6241	0.0309	32.7265
2.0	0.6525	0.0387	−0.0840	8.5253	0.0734	26.0018
2.5	0.6576	0.0383	−0.1974	8.3847	0.1148	20.3461
3.0	0.6605	0.0376	−0.1962	8.2066	0.1640	16.0260
3.5	0.6625	0.0384	−0.0793	8.1357	0.2018	13.2581
4.0	0.6634	0.0388	0.0086	7.9881	0.2359	10.8769
4.5	0.6644	0.0390	0.0081	7.9333	0.2531	9.2102
5.0	0.6647	0.0386	−0.0527	7.8750	0.2622	7.9085
10.0	0.6662	0.0416	0.2482	7.9177	0.3342	4.4610
DEV						
1.0	0.6389	0.0363	−0.0954	8.6689	0.0281	46.0916
1.3	0.6427	0.0405	0.1771	8.6137	0.0249	42.2059
1.5	0.6444	0.0399	0.1223	8.5451	0.0476	39.7536
2.0	0.6500	0.0387	−0.0215	8.4097	0.0744	27.1618
2.5	0.6557	0.0396	0.0594	8.3101	0.1028	19.4110
3.0	0.6587	0.0396	0.0924	8.1634	0.1453	15.2955
3.5	0.6599	0.0386	0.0382	7.9801	0.1881	12.3952
4.0	0.6609	0.0388	0.0744	7.8672	0.2131	9.8732
4.5	0.6614	0.0393	0.1539	7.7965	0.2336	8.5445
5.0	0.6620	0.0396	0.1793	7.4895	0.2492	7.3233
10.0	0.6634	0.0419	0.3617	7.7373	0.3114	3.8805

References

Ai, J., Chen, J.-F., & Ooi, J. Y. (2013). Finite element simulation of the pressure dip in sandpiles. *International Journal of Solids and Structures*, *50*(6), 981–995.

Alonso-Marroquin, F., Luding, S., Herrmann, H. J., & Vardoulakis, I. (2005). Role of anisotropy in the elastoplastic response of a polygonal packing. *Physical Review E*, *71*(5), 051304.

Anderson, D. A. (1996). Influence of fines on performance on asphalt concrete mixtures. In *Proceedings ICAR 4th Annual Symposium*

Azéma, E., & Radjaï, F. (2012). Force chains and contact network topology in sheared packings of elongated particles. *Physical Review E*, *85*(3), 031303.

Azéma, E., Radjaï, F., & Saussine, G. (2009). Quasistatic rheology, force transmission and fabric properties of a packing of irregular polyhedral particles. *Mechanics of Materials*, *41*(6), 729–741.

Bauer, E., Huang, W., & Wu, W. (2004). Investigations of shear banding in an anisotropic hypoplastic material. *International Journal of Solids and Structures*, *41*(21), 5903–5919.

Belkhatir, M., Arab, A., Della, N., & Schanz, T. (2012). Experimental study of undrained shear strength of silty sand: Effect of fines and gradation. *Geotechnical and Geological Engineering*, *30*(5), 1103–1118.

Belkhatir, M., Arab, A., Schanz, T., Missoum, H., & Della, N. (2011). Laboratory study on the liquefaction resistance of sand–silt mixtures: Effect of grading characteristics. *Granular Matter*, *13*(5), 599–609.
Bi, D., Zhang, J., Chakraborty, B., & Behringer, R. P. (2011). Jamming by shear. *Nature*, *480*(7377), 355–358.
Cui, L., & O'Sullivan, C. (2006). Exploring the macro- and micro-scale response of an idealised granular material in the direct shear apparatus. *Géotechnique*, *56*(7), 455–468.
Cundall, P. A., & Strack, O. D. L. (1979). A discrete numerical model for granular assemblies. *Géeotechnique*, *29*(1), 47–65.
Dodds, P. S., & Weitz, J. S. (2002). Packing-limited growth. *Physical Review E*, *65*(5), 056108.
Durán, O., Kruyt, N. P., & Luding, S. (2010). Micro-mechanical analysis of deformation characteristics of three-dimensional granular materials. *International Journal of Solids and Structures*, *47*(17), 2234–2245.
Einav, I. (2012). The unification of hypo-plastic and elasto-plastic theories. *International Journal of Solids and Structures*, *49*(11–12), 1305–1315.
Goddard, J. D. (1998). Continuum modeling of granular assemblies. In H. J. Herrmann, J. P. Hovi, & S. Luding (Eds.), *Physics of dry granular media—NATO ASI Series E 350* (pp. 1–24). Dordrecht: Kluwer Academic Publishers.
Goddard, J. D. (2006). A dissipative anisotropic uid model for non-colloidal particle dispersions. *Journal of Fluid Mechanics*, *568*(1), 1-17.
Goddard, J. D. (2010). Parametric hypoplasticity as continuum model for granular media: From Stokesium to Mohr-Coulombium and beyond. *Granular Matter*, *12*(2), 145-150.
Göncü, F., Duran, O., & Luding, S. (2010). Constitutive relations for the isotropic deformation of frictionless packings of polydisperse spheres. *Comptes Rendus Mécanique*, *338*(10–11), 570–586.
Göncü, F., & Luding, S. (2013). Effect of particle friction and polydispersity on the macroscopic stress–strain relations of granular materials. *Acta Geotechnica*, *8*(6), 629–643.
Hanley, K. J., O'Sullivan, C., Byrne, E. P., & Cronin, K. (2012). Discrete element modelling of the quasi-static uniaxial compression of individual infant formula agglomerates. *Particuology*, *10*(5), 523–531.
Hareb, H., & Doanh, T. (2012). Probing into the strain induced anisotropy of Hostun RF loose sand. *Granular Matter*, *14*(5), 589–605.
Imole, O. I., Kumar, N., Magnanimo, V., & Luding, S. (2013). Hydrostatic and shear behavior of frictionless granular assemblies under different deformation conditions. *KONA*, *30*, 84–108.
Imole, O. I., Wojtkowski, M. B., Kumar, N., Magnanimo, V., & Luding, S. (2013). Force correlations, anisotropy and friction mobilization in granular assemblies under uniaxial deformation. In S. Luding, & A. Yu (Eds.), *Powders & Grains 2013* (pp. 601–604). Amsterdam: Balkema. Sydney, Australia.
Ji, S., & Shen, H. H. (2006). Effect of contact force models on granular flow dynamics. *Journal of Engineering Mechanics*, *132*(11), 1252–1259.
Jiang, Y., & Liu, M. (2007). From elasticity to hypoplasticity: Dynamics of granular solids. *Physical Review Letters*, *99*, 105501.
Kolymbas, D., Herle, I., & von Wolffersdorff, P. A. (1995). Hypoplastic constitutive equation with internal variables. *International Journal for Numerical and Analytical Methods in Geomechanics*, *19*(6), 415–436.
Krijgsman, D., & Luding, S. (2013). 2D cyclic pure shear of granular materials, simulations and model. In S. Luding, & A. Yu (Eds.), *Powders & Grains 2013* (pp. 1226–1229). Amsterdam: Balkema. Sydney, Australia.
Kruyt, N. P., Agnolin, I., Luding, S., & Rothenburg, L. (2010). Micromechanical study of elastic moduli of loose granular materials. *Journal of the Mechanics and Physics of Solids*, *58*(9), 1286–1301.
Kumar, N., Imole, O. I., Magnanimo, V., & Luding, S. (2013). Evolution of the effective moduli for anisotropic granular materials during shear. In S. Luding, & A. Yu (Eds.), *Powders & Grains 2013* (pp. 1238–1241). Amsterdam: Balkema. Sydney, Australia.
Kwade, A., Schulze, D., & Schwedes, J. (1994a). Determination of the stress ratio in uniaxial compression tests—Part 1. *Powder handling & Processing*, *6*(1), 61–65.
Kwade, A., Schulze, D., & Schwedes, J. (1994b). Determination of the stress ratio in uniaxial compression tests—Part 2. *Powder handling & Processing*, *6*(2), 199–203.
La Ragione, L., & Magnanimo, V. (2012). Contact anisotropy and coordination number for a granular assembly: A comparison of distinct-element-method simulations and theory. *Physical Review E*, *85*(3), 031304.
Luding, S. (2004). Micro–macro models for anisotropic granular media. In P. A. Vermeer, W. Ehlers, H. J. Herrmann, & E. Ramm (Eds.), *Modelling of cohesive-frictional materials* (pp. 195–206). Leiden: Balkema.
Luding, S. (2005a). Anisotropy in cohesive, frictional granular media. *Journal of Physics: Condensed Matter*, *17*(24), S2623–S2640.
Luding, S. (2005b). Shear flow modeling of cohesive and frictional fine powder. *Powder Technology*, *158*(1–3), 45–50.
Luding, S. (2008). Cohesive, frictional powders: contact models for tension. *Granular Matter*, *10*(4), 235–246.
Luding, S., & Perdahcıoğlu, E. S. (2011). A local constitutive model with anisotropy for various homogeneous 2D biaxial deformation modes. *Chemie Ingenieur Technik*, *83*(5), 672–688.
Madadi, M., Tsoungui, O., Lätzel, M., & Luding, S. (2004). On the fabric tensor of polydisperse granular materials in 2D. *International Journal of Solids and Structures*, *41*(9–10), 2563–2580.
Magnanimo, V., & Luding, S. (2011). A local constitutive model with anisotropy for ratcheting under 2D axial-symmetric isobaric deformation. *Granular Matter*, *13*(3), 225–232.
Majmudar, T. S., Sperl, M., Luding, S., & Behringer, R. P. (2007). Jamming transition in granular systems. *Physical Review Letters*, *98*(5), 058001.
Makse, H. A., Johnson, D. L., & Schwartz, L. M. (2000). Packing of compressible granular materials. *Physical Review Letters*, *84*(18), 4160–4163.
Mašín, D. (2012). Asymptotic behaviour of granular materials. *Granular Matter*, *14*(6), 759–774.
MiDi, G. D. R. (2004). On dense granular flows. *European Physical Journal E: Soft Matter*, *14*(4), 367–371.
Morgeneyer, M., & Schwedes, J. (2003). Investigation of powder properties using alternating strain paths. *Task Quarterly*, *7*(4), 571–578.
Oda, M. (1972). Initial fabrics and their relations to mechanical properties of granular materials. *Soils and Foundation*, *12*(1), 17–36.
Ogarko, V., & Luding, S. (2012). Equation of state and jamming density for equivalent bi- and polydisperse, smooth, hard sphere systems. *Journal of Chemical Physics*, *136*(12), 124508.
Ogarko, V., & Luding, S. (2013). Prediction of polydisperse hard-sphere mixture behavior using tridisperse systems. *Soft Matter*, *9*(40), 9530–9534.
O'Hern, C. S., Langer, S. A., Liu, A. J., & Nagel, S. R. (2002). Random packings of frictionless particles. *Physical Review Letters*, *88*(7), 075507.
Peyneau, P.-E., & Roux, J.-N. (2008). Solidlike behavior and anisotropy in rigid frictionless bead assemblies. *Physical Review E*, *78*(4), 041307.
Radjaï, F., Roux, S., & Moreau, J. J. (1999). Contact forces in a granular packing. *Chaos*, *9*(3), 544–550.
Satake, M. (1982). Fabric tensor in granular materials. In P. A. Vermeer, & H. J. Luger (Eds.), *Proceedings of the IUTAM Symposium on Deformation and Failure of Granular materials* (pp. 63–68). Delft, The Netherlands, Rotterdam: A.A. Balkema.
Schröder-Turk, G. E., Mickel, W., Schröter, M., Delaney, G. W., Saadatfar, M., Senden, T. J., et al. (2010). Disordered spherical bead packs are anisotropic. *Europhysics Letters*, *90*(3), 34001.
Shaebani, M. R., Madadi, M., Luding, S., & Wolf, D. E. (2012). Influence of polydispersity on micromechanics of granular materials. *Physical Review E*, *85*(1), 011301.
Shäfer, J., Dippel, S., & Wolf, D. E. (1996). Force schemes in simulations of granular materials. *Journal de Physique I (France)*, *6*(1), 5–20.
Sun, J., & Sundaresan, S. (2011). A constitutive model with microstructure evolution for flow of rate-independent granular materials. *Journal of Fluid Mechanics*, *682*, 590–616.
Tejchman, J., & Wu, W. (2007). Modeling of textural anisotropy in granular materials with stochastic micro-polar hypoplasticity. *International Journal of Non-Linear Mechanics*, *42*(6), 882–894.
Thornton, C. (2010). Quasi-static simulations of compact polydisperse particle systems. *Particuology*, *8*(2), 119–126.
Thornton, C., & Zhang, L. (2006). A numerical examination of shear banding and simple shear non-coaxial flow rules. *Philosophical Magazine*, *86*(21–22), 3425–3452.
Thornton, C., & Zhang, L. (2010). On the evolution of stress and microstructure during general 3D deviatoric straining of granular media. *Géotechnique*, *60*(5), 333–341.
Tomas, J. (2001). Assessment of mechanical properties of cohesive particulate solids. Part 1: Particle contact constitutive model. *Particulate Science and Technology*, *19*, 95–110.
van Hecke, M. (2010). Jamming of soft particles: Geometry, mechanics, scaling and isostaticity. *Journal of Physics: Condensed Matter*, *22*(3), 033101.
Voivret, C., Radjaï, F., Delenne, J. Y., & El Youssoufi, M. S. (2007). Space-filling properties of polydisperse granular media. *Physical Review E*, *76*(2), 021301.
Voivret, C., Radjaï, F., Delenne, J. Y., & El Youssoufi, M. S. (2009). Multiscale force networks in highly polydisperse granular media. *Physical Review Letters*, *102*(17), 178001.
Walsh, S. D. C., & Tordesillas, A. (2004). A thermomechanical approach to the development of micropolar constitutive models of granular media. *Acta Mechanica*, *167*(3), 145–169.
Zetzener, H., & Schwedes, J. (1998). Deformation behaviour and relaxation of bulk solids at different deformation rates. In *Proceedings of the 6th International Conference on Bulk Materials Storage, Handling and Transportation* Wollongong, Australia, (pp. 51–55).